Chapter 2

Conceptual framework and summary of literature

The first part of this chapter gives a short introduction to the molecular dynamics simulations of halogens in rare gas solids based on a classical picture of the system. A semiclassical extension to this theory is presented which provides the most detailed description of the dynamical system at present.
The literature will be summarized with the focus on the special systems, that are experimentally examined with femtosecond pulses for the first time in this thesis, ClF and Cl_2 in Ar and Kr matrices. The introduction to fs-pump-probe spectroscopy is given with an emphasis on dissipative systems. A nearly complete summary of the literature concerning the spectroscopy of the molecule ClF is given.

2.1 Simulations of ultrafast dynamics in condensed phase

2.1.1 Classical molecular dynamics: I_2/Kr and F_2/Ar

The early classical molecular dynamics simulations of I_2/Kr and F_2/Ar already demonstrate many of the important dynamical effects discussed in this thesis. The simulations start with a box of approx. 500 rare gas (Rg) atoms in a closest packed geometry (face centered cubic - fcc), with a halogen molecule (Y_2) in the center of the box. A small molecule like F_2 occupies only one lattice site (substitutional) of the solid and large molecules like I_2 occupy two lattice sites (double substitutional). The forces between two rare gas atoms ($Rg - Rg$) and between halogen and rare gas $Y - Rg$ are of the van-der-Waals type, with strong repulsion at short distances and weak attraction, i.e. nearly a system of hard spheres. For the molecular $Y - Y$ interaction, a Morse potential is used and potentials are assumed to be pairwise additive. In this classical system, the dynamics correspond to three dimensional billiards.

To describe the photodynamics of the molecules, first the initial conditions have to be found. The system is equilibrated at a specified temperature with the molecule in its ground state X. The initial configurations are then randomly sampled under the condition that the molecular bond distance R fulfills the Franck resonance condition [104] with the excited electronic state within the energy bandwidth of the pump pulse. The trajectories are then started for each of the initial conditions by switching the molecular potential from the ground state (X) to the excited state. Since the system is entirely classical, the positions and momenta of all particles can be calculated for each time step by numerical propagation of Hamilton's equations.

Classical trajectories for I_2/Kr from ref. [26]

First consider the photodynamics of the large and heavy I_2 molecule, excited to its A state[1] above the gas phase dissociation limit, in the center of a box of Kr atoms [26]. Fig. 2.1a shows the bond distance R_{I-I} as a function of time t for a set of trajectories. All trajectories start well localized at

[1] A is the lowest optically accessible state of I_2 with a shallow potential (weak binding).

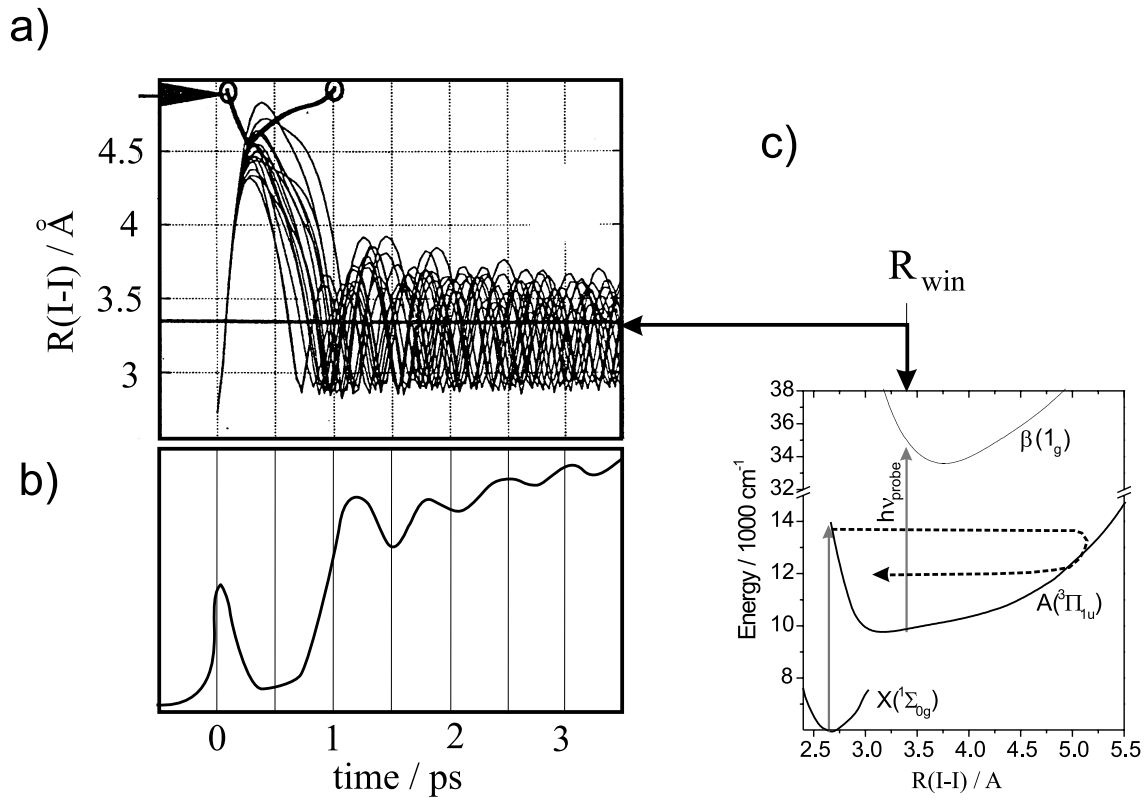

Figure 2.1: a) Bond distance R_{I-I} as a function of time from classical trajectory calculations of I_2/Kr. Each line corresponds to one trajectory for a given initial condition. b) Experimental pump-probe spectrum for $\lambda_{pump} = 704$ nm and $\lambda_{probe} = 352$ nm. c) Potential energy diagram of I_2 with probe window at R_{win} from the A state to the ion-pair states, which connects the trajectories with the observed signal [26].

$R_{I-I} = 0.266$ nm. The bond stretches to 0.45 nm within 300 fs, and here the I atoms encounter the Kr cage atoms, suddenly stopping the dissociative motion. In all trajectories, the I atoms are forced to recombine within 1 ps and subsequently oscillate around the new equilibrium bond length near 0.33 nm. The slightly different initial conditions, i.e. positions and momenta of the two I atoms and all Kr atoms, prepare different scattering parameters, yielding a very broad distribution of recombining trajectories. The strong energy loss in the first collision can is evident from the reduced amplitude of the $I - I$ oscillations in the molecular potential.

Fig. 2.1c depicts the potential diagram which connects the simulated trajectories with the observed signal in a pump-probe spectrum in panel b). The energy $h\nu$ of the probe pulse specifies the probe window R_{win} by the Franck-Condon resonance (*chapter 2.9*) to a higher lying state. The intensity of the fluorescence from this state is proportional to the number of trajectories in the probe window during the time interval of the probe pulse. A high velocity of the trajectories decreases the signal, because the trajectory spends less time in the probe window.

Fig. 2.2 shows the ensemble averaged total energy of I_2 for the trajectories from Fig. 2.1a. A rapid loss of 2000 cm^{-1} within the first ps, induced by the first strong fragment-cage collisions after dissociation, is followed by a slow exponential decay for the vibrational relaxation after recombination in the A state.

In *chapter 7.3.1* an $I - I$ trajectory vibrationally relaxing in the B state will be derived from the pump-probe spectra and *chapter 7.4.2* presents the corresponding relaxation rates. The energy loss in the A state is discussed in *chapter 7.4.3*.

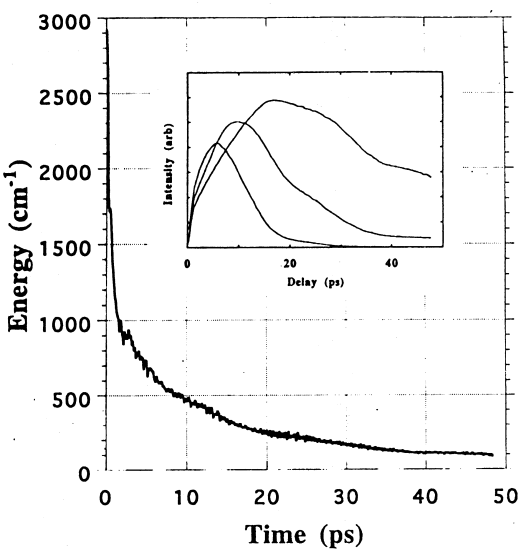

Figure 2.2: Ensemble averaged total energy of I_2 as a function of time [26]. An initial rapid loss is followed by a slow exponential decay with time constant 12 ps. The inset shows the pump-probe spectra calculated from the same ensemble for three different window locations a) 0.35 nm, b) 0.34 nm and c) 0.33 nm. The smaller R_{win} is located deeper in the potential and sees the population for longer times.

Classical trajectories for F_2/Ar from ref. [67]

While even at high excess energies, the I atoms are always confined to the initial cage in a Kr solid, the observed behavior for F_2 in Ar solids is entirely different. Classical trajectory calculations [67] on F_2/Ar predict that F atoms leave the cage around the F_2 molecule, formed by the first Ar shell. This cage exit is observed in 55% of trajectories already at an excess energy $E_{excess} = 1$ eV of the molecule above its gas phase dissociation limit. Fig. 2.3a) shows a typical trajectory for excitation of F_2 in the $^1\Pi$ state[2] with $E_{excess} = 1$ eV. The trajectory shows asymmetric cage exit, i.e. one F atom (1) leaves the original cage and the other one (2) resides on the initial substitutional site. Panel a) shows the distance of both atoms to their initial position as a function of time. Fragment 1 encounters an Ar atom after 500 fs which forces the F atom to stay in the original cage. After approx. 1 ps, the F atom suddenly hops out of the cage and is trapped in the nearest interstitial site[3] (cf. Fig. 2.5c). Fragment 2, in contrast, is confined to the original substitutional site. Panel b) displays the kinetic energies of the two particles. The kinetic energy of both particles is rapidly lost, however, after 1 ps atom 1 picks up 0.1 eV of kinetic energy after overcoming the barrier for dissociation. Again, this energy is quickly dissipated in the final (interstitial) site.

The probability for cage exit increases with the excitation energy. For excess energies higher than 1 eV the symmetric cage exit dominates (both fragments leave the cage). The initial configuration plays an important role, and at low temperatures (4 K) the $F - F$ atom is initially aligned with both F atoms pointing at triangular windows of the cage (cf. Fig. 2.5c), which again favors cage exit.

The small size of the F fragments determines the recombination dynamics, as well. The molecular $F - F$ bond may be rapidly tilted by scattering off the cage atoms, as is observed in the trajectory plotted in Fig. 2.4. In contrast, the $I - I$ bond orientation is sterically fixed by the solid Kr lattice.

The fs-pump-probe spectra of ClF in Ar will display the recombination dynamics *(chapter 7.3.2)*, the energy loss by vibrational relaxation *(chapter 7.4.3)*, the tilting of the $Cl - F$ bond *(chapter 7.5.3)* and the cage exit of F fragments (*chapter 7.7*).

[2]The lowest allowed transition from the ground state of the F_2 molecule is to the $^1\Pi$ state, which is purely repulsive.
[3]interstitial = opposite of substitutional = between the atoms of a complete lattice

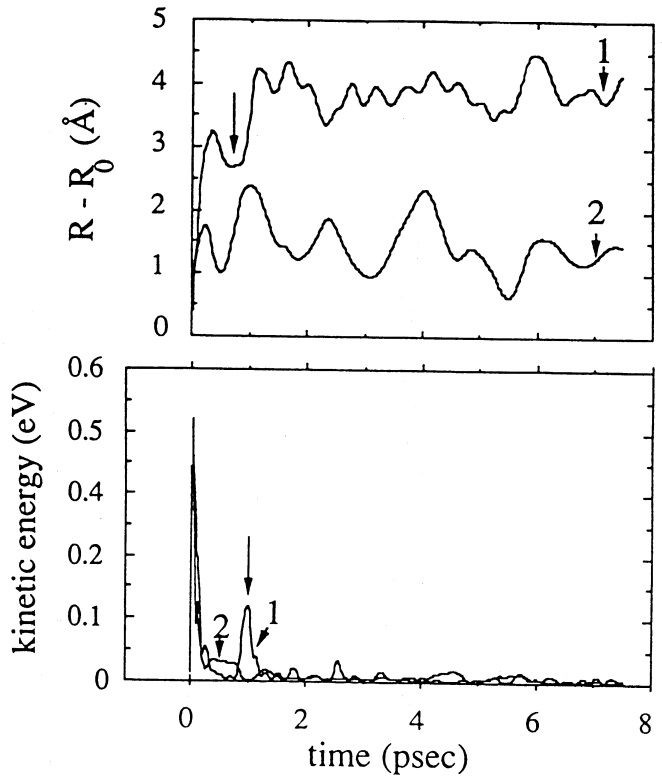

Figure 2.3: a) Distance of the two F fragments to their initial position as a function of time from classical trajectory simulations on F_2/Ar photodissociation. A single trajectory is shown that shows asymmetric cage exit. b) Corresponding kinetic energies of the two F fragments as a function of time [67].

2.1.2 Coupling of electronic and nuclear motion

The classical molecular dynamics (MD) on a single electronic potential energy surface deliver many details of the photodynamical processes, which can be described by classical quantities of the nuclei, such as position, momentum, kinetic energy, bond-direction and cage exit probability. The processes will be described correctly as long as only one electronic state is involved in the dynamics (weak electronic coupling). Recombination to the ground state or other bound electronic states alter the dynamics and compete with the cage exit. Changes of electronic state decrease the probability of cage exit, especially, if repulsive states are initially excited.

Transitions among coupled electronic states of a molecule give rise to non-adiabatic dynamics, i.e. coupled motion of electronic and nuclear degrees of freedom. The adiabatic approximation (Born-Oppenheimer approximation) assumes that the motion of electrons is much faster than the motion of nuclei. As a consequence, the electron configuration should instantaneously adjust to the position of the nuclei. The electronic state determines the dynamics, since it sets the forces on the nuclei as the gradient of the potential energy. The nuclear motion in turn influences the coupling of electronic states, i.e. the probability for changing the occupation of the electronic states. In the semi-classical Landau-Zener picture[4], the transition probability w depends on the velocity v of the trajectory $w = 1 - \exp(-A/v)$. Thus, nuclear and electronic degrees of freedom are coupled.

Non-adiabatic coupling arises from the anisotropic interaction energy of the open shell fragments (P-orbitals) with a rare gas atom, as well. It is given by $U^{DIM}(r_i,\gamma_i) = V_0(r_i) + V_2(r_i)P_2(\cos\gamma_i)$, where V_o is the isotropic part of the interaction potential and V_2, together with the second Legendre polynomial, describes the angular dependence of the asymmetric part [107]. This interaction, based

[4]The constant A in the exponential is given as $A = 2\pi V_x^2/(\hbar|F_2 - F_1|)$, where V_x^2 is the coupling matrix element of the two states and $|F_2 - F_1|$ is the difference of the forces according to the two potential surfaces at the crossing [105, 106].

In a quantum mechanical picture, the overlap of the vibrational wave functions determines the transition probability. The vibrational states are the solutions of Schrödinger's equation for the nuclear motion.

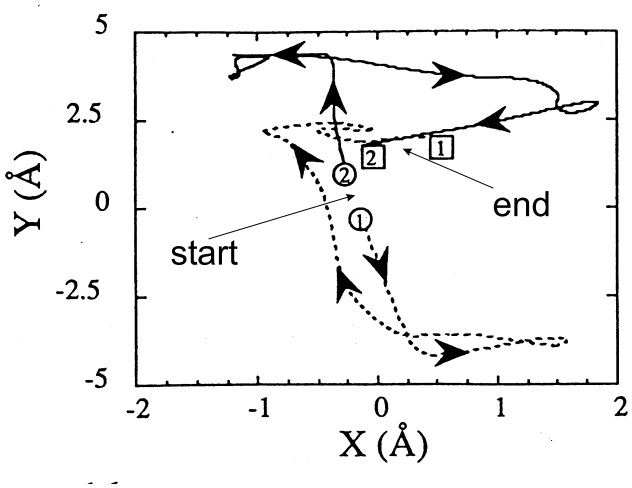

Figure 2.4: Nonreactive trajectory of both F fragments (1 and 2) in two cartesian coordinates [67]. The initial positions are denoted as circles, the final positions after 3.5 ps as squares. At the end of this recombination dynamics, the $F-F$ bond is tilted by 90°.

on electrostatic and empirical considerations, is clearly not of the Born-Oppenheimer type. It explicitly depends on an electronic degree of freedom, the orbital angle γ_i. Pictorially speaking, the lobes of the electronic orbitals are attached to the nucleus and may be tilted by the dynamical interaction with the electron clouds of the rare gas atoms. An adiabatic vs. nonadiabatic treatment of the problem is compared in ref. [69, 70].

2.1.3 DIM and DIIS treatment for potential energy surfaces

To handle nonadiabatic processes, first, an efficient calculation of the electronic surfaces is needed that can be included in dynamical simulations. The diatomics-in-molecules (DIM) method is a semi-empirical approach developed by Ellison [108] for computing potential energy surfaces (PES) of polyatomic systems from diatomic potentials. A detailed explanation of this method is exemplified in the system I_2/Rg [63–65]. It is an extension of the simple approach of adding up pair potentials presented in chapter 2.2.4, that also accounts for the proper symmetrization of the electronic wave functions. The molecular interactions, e.g. of Cl with F will distort the electron distribution of these atoms, and thus the interaction with the surrounding Ar atoms is altered, too. The idea is to cast the total Hamiltonian into a form which contains only Hamiltonians of all possible diatomic and monatomic constituents, but no interaction operators. Thereby, experimental diatomic and monatomic energies can be taken as the eigenenergies after diagonalization of the matrix. DIM uses the pair potentials as a starting point, and it is not surprising that it works best for weakly bound molecular states, since for these the deformation of the electronic clouds is weak [109].

For halogens and interhalogens a total number of 36 valence states has to be taken into account, because 13 of the 23 electronic states have $\Omega \neq 0$ and are doubly degenerate. The surrounding rare gas atoms break the symmetry of the molecular states of $F-F$ or $Cl-F$, and the direction – not only the absolute value of the projection of the angular momentum – enters into the potential energy. For a detailed modeling, spin-orbit interaction must be taken into account. It was shown that spin-non-conserving transitions play a crucial role in the dynamics [71] (*chapter 7.6*).

The diatomics-in-ionic-systems (DIIS) method is a variant of the DIM method that also accounts for the coupling of electron-transfer (ion-pair) states with neutral valence states. It has been pioneered by Last and George [110, 111] for Cl/Xe and successfully applied by Batista and Coker for I_2/Kr.

For a detailed explanation of the DIM and DIIS method, the reader is referred to the literature cited above and to ref. [112].

2.1.4 Non-adiabatic molecular dynamics (DIM - trajectories)

A very fruitful way of treating molecular dynamics on several electronic surfaces semiclassically, is the "surface hopping" method developed by Tully and co-workers, which treats nuclear motions classically and the electronic degrees of freedom quantum-mechanically [113, 114]. Criteria based on the time dependence of the electronic wave functions are used in an algorithm that decides when the "hopping" to another electronic state takes place.

DIM-trajectory simulations combine the calculation of electronic PES by the DIM method with the semi-classical surface-hopping technique [63–65, 71]. In each time step, the Hamiltonian is diagonalized in the electron coordinates, and the eigenvalues yield the energies of all electronic states for the specific nuclear configuration at time t. The new potential delivers the forces on the nuclear degrees of freedom for the next time step. The nuclei are treated classically, and the position of all particles is known for all times. It is common to plot the position of the relevant particles for individual trajectories and to display the eigenvalues of the Hamiltonian, i.e. the potential energy for all electronic states as a function of time (e.g. Fig. 7.19).

The zero-point motion of the atoms must be added artificially to the initial conditions in an appropriate way. The classical approximation is especially good if the atoms are either heavy or hot. The spreading of the wave packet will be discussed in the following chapter, and it will enter in the discussion of the ClF wave packets *(chapter 7.3.2)*. There are several ways to incorporate wave properties of matter in MD trajectory simulations [102, 103].

DIM trajectories for I_2/Kr

It is well known that the bound B state of I_2 is coupled to repulsive electronic states. This predissociation is strongly enhanced in condensed phase and the major aim of the DIM studies was to quantitatively simulate the corresponding nonadiabatic dynamics. The predissociation of I_2 will not be considered in this thesis, since in solid Kr it takes place on a timescale of 10 ps [115, 116]. The discussion will focus on the description of the early B state dynamics itself and the strong interaction with the Kr environment. A one dimensional representation of the multidimensional potential will be constructed from the experiment, and the discussion in *chapter 7.1* will show that an average over potential energies from many DIM trajectories is desirable for comparison. An ensemble average, together with a width of the distribution for the classical quantities, would display an intuitive semiclassical picture of a wave packet smeared out in phase space. *Fig. 7.7b* demonstrates the discussed effects for a trajectory of I_2/Ar, but for a quantitative evaluation, simulations of the system I_2/Kr are needed.

DIM trajectories for F_2/Rg

The nonadiabatic simulations of the dynamics of F_2 in Rg add several very interesting predictions to the classical results. Ref. [71] presents simulations of the non-adiabatic dynamics of F_2 in an Ar_{54} cluster after excitation to the singlet $^1\Pi$ state. The main result is the ultrafast transition to the weakly bound $^3\Pi$ states, involving an ultrafast spin-flip, that will be discussed in *chapter 7.6*. The dissociation quantum efficiency is lower in the nonadiabatic simulations, and ref. [71] emphasizes the importance of delayed cage exit at low excitation energies, i.e. the process displayed in Fig. 2.3. The F atom first kicks the argon atoms, and can only exit after the cage has opened after approx. 1 ps. In the MD simulations of F in Kr it was observed, that the kinetic energy of the nuclei can be transferred to electronic potential energy, which reduces the probability to overcome the potential barriers [69, 70].

2.1.5 Wave packets

This chapter is a quick reminder of some important features of wave packets. For further reading consider refs. [117] and [118].

Wave packets are a coherent superposition of several eigenstates of a quantum system. The excitation of a diatomic molecule with a sufficiently short fs-pump-pulse prepares a coherent superposition of vibrational levels with the time dependent wave function $\psi(R,t)$, where R is the bond length and t is time. If the square of the wave function $|\psi(R,t)|^2$ is localized in the coordinate R, this is called a wave packet. The spatial width of the wave packet corresponds to the uncertainty for a measurement of the bond distance, i.e. the location of the constituent atoms is smeared out.

In the cold rare gas matrix, initially the vibrational ground state is populated, and the wave function is a Gaussian. A short laser pulse projects this Gaussian wave function onto the excited state surface, and in the linear approximation of the excite state potential its shape remains Gaussian [117].

The spatial and energetic width of the I_2 wave packet is examined in *chapter 7.2* and the dispersion of the $Cl-F$ wave packet is discussed in *chapter 7.3.2*.

Dynamics and spreading of the wave packet

The wave packet obeys Schrödinger's equation $i\hbar\frac{\partial}{\partial t}\Psi(R,t) = \left(\frac{p^2}{2m} + U(R)\right)\Psi(R,t)$ in the potential $U(R)$. With Ehrenfest's theorems [101], it is transformed into the differential equations for the expectation values $\langle R\rangle$ for space and $\langle p\rangle$ for momentum.

$$\frac{\partial}{\partial t}\langle R\rangle = \frac{\langle p\rangle}{m}; \frac{\partial}{\partial t}\langle p\rangle = -\langle \nabla U(R)\rangle \tag{2.1}$$

They govern the classical trajectory of the wave packet. For some potentials the expectation value of the gradient of the potential is equal to the gradient of the potential at the expectation value $\langle R\rangle$, i.e. $\langle \nabla U(R)\rangle = \nabla_{\langle R\rangle} U(\langle R\rangle)$. Then eq. 2.1 are the classical Hamilton equations for the expectation value $\langle R\rangle$. This is true for all linear and quadratic potentials and Ehrenfest's description of the wave packet motion becomes exact.

$$\langle \partial U(R)/\partial R\rangle = \left\langle \partial R^2/\partial R\right\rangle \stackrel{!}{=} \langle 2R\rangle \stackrel{!}{=} \partial \langle R\rangle^2 / \partial\langle R\rangle = \partial U(\langle R\rangle)/\partial\langle R\rangle .$$

The classical equations are approximated by eq. 2.1 if the wave packet is well localized and the potential is nearly constant within the spread of the wave packet ($\nabla U(R) \approx \nabla U(r)|_{r=\langle R\rangle}$). Then the constant gradient of the potential can be taken out of the integral.

$$\langle \nabla U(R)\rangle = \int \Psi^* [\nabla U(R)]\Psi dR \approx \nabla_{\langle R\rangle} U(\langle R\rangle). \tag{2.2}$$

Under the influence of the potential, the width ΔR of the packet changes in time, and this is called dispersion[5]. For a freely propagating Gaussian ($U = const.$) in a constant potential, the width changes according to $\Delta R(t) = \sqrt{R^2 - \langle R\rangle^2} = \sigma\sqrt{1 + t^2\left(\hbar/2m\sigma^2\right)^2}$, with $\sigma = \Delta R(0)$. For large t, the width grows linearly with time according to $\Delta R(t)/\sigma = t\frac{\hbar}{2m\sigma^2}$. Consider excitation to the repulsive ClF potential surface with a bandwidth of 500 cm^{-1}. The spatial width of the wave packet excited by this pulse is $\sigma = 0.008$ nm. A freely propagating ClF wave packet (taking the ClF potential as flat) with this width and reduced mass $m = 12.3$ amu would double after $t = 4m\sigma^2/\hbar = 50$ fs. For an I_2 wave packet with the same initial spacial width but with reduced mass $m = 127$ amu the time increases to 500 fs.

The harmonic potential is the only case where wave packets do not disperse and keep their shape. If a Gaussian ground state wave packet is transferred to a potential with the same shape, the wave packet will oscillate without changing shape (coherent state). If the new potential is flatter, but still harmonic, the wave packet will get broader near the minimum and return to its original shape at the

[5] Unfortunately sometimes also the word "dephasing" is used, but this is an ambiguous term as discussed in chapter 2.3.3.

turning point. If the potential is steeper, the wave packet is focused near the minimum, however in the same way in each period [117].

The dynamics in a more realistic, anharmonic Morse potential is similar. The laser pulse prepares the wave packet at its turning point in the Morse oscillator. In diatomic molecules the excited states are in general more weakly bound, and thus, the sharp Gaussian ground state wave packet broadens near the minimum of the excited state but gets sharper at the outer turning point. The anharmonicity changes the shape of the wave packet from period to period by dispersion. The dispersion of the wave packet may be pre-compensated by chirping the pump pulse, i.e. exciting the slower moving components first [19, 31, 32]. For this pre-compensation no discrete structure of vibrational levels is needed. Also classical particles in an anharmonic potential have different round-trip times. When the slower particles are started first, the faster ones can catch up with them, and all particles will be focused (piled up) after a certain time. In this sense the effect is classical.

When the wave packet is prepared with a transform limited (not chirped) pulse, it will spread out. After some time determined by the vibrational frequency and anharmonicity of the potential, the wave packet displays so-called partial and complete revivals (rephasing) and the dynamics start all over again. For the revivals a discrete structure of energy levels is needed and the effect is thus quantum mechanical. Consider for example three levels, with different round-trip times $T - \Delta T$, T and $T + \Delta T$. After a (large) number N of round-trips, $N\Delta T = T$ and the levels are back "in phase". For a higher number of excited levels, this is only a partial revival and the complete rephasing is even later. In the B state of I_2 this time is on the order of 50 ps. In the condensed phase considered here, the "rephasing time" due to the anharmonicity is long compared to the timescale for the destruction of the phases by random scattering off the bath atoms, and this process was never observed. From a different viewpoint, the fluctuating environment smears out the vibrational level structure, which destroys the coherence. The measured data are analyzed with respect to vibrational coherence in *chapter 7.9*.

Classical oscillation in a Morse potential

For heavy molecules like I_2 the classical approximation is good since the large mass prevents a fast spreading of the wave function. Morse potentials are close approximations to realistic molecular potentials $V(R) = D_e \left(1 - e^{-\beta_m (R-R_e)}\right)^2$. In *chapter 5.3*, a Morse-like extrapolation is used to construct an effective one dimensional potential for I_2/Kr. The classical vibrational frequency of a Morse oscillator is

$$\nu_{morse}\,(E) = \omega_e \sqrt{1 - \frac{E}{D_e}}, \tag{2.3}$$

with the harmonic frequency $\omega_e = \beta_m \sqrt{2D_e/m}$. D_e is the dissociation energy and m the reduced mass. ω_e is a frequency (not angular frequency) but is usually measured in wavenumbers (cm^{-1}) like the energies E and D_e. The anharmonicity $\omega_e x_e = \frac{1}{2}\nu \, d\nu/dE$ of the Morse potential is constant, independent of E.

$$\frac{d\nu_{morse}}{dE} = -\frac{\omega_e}{2D_e}\left(1 - \frac{E}{D_e}\right)^{-\frac{1}{2}} = -\frac{\omega_e^2}{2D_e\nu_{morse}} \tag{2.4}$$

If a wave packet is excited with a spectral bandwidth of ΔE and without chirp, it will disperse due to the anharmonicity $\omega_e x_e$. The wave packet will be smeared out after n periods, when the differences of vibrational frequencies $\Delta\nu_{morse}$ have accumulated $n\Delta\nu_{morse} = \nu_{morse}$. Here $\Delta\nu_{morse}$ is defined as the frequency difference at the full width half maximum of the excitation pulse ΔE.

$$n = \frac{\nu_{morse}^2}{2\Delta E \omega_e x_e} \tag{2.5}$$

A larger anharmonicity $\omega_e x_e$ and a broader excitation spectrum ΔE lead to a faster dispersion of the wave packet. As an example consider a wave packet on ClF/Ar near the dissociation limit, where

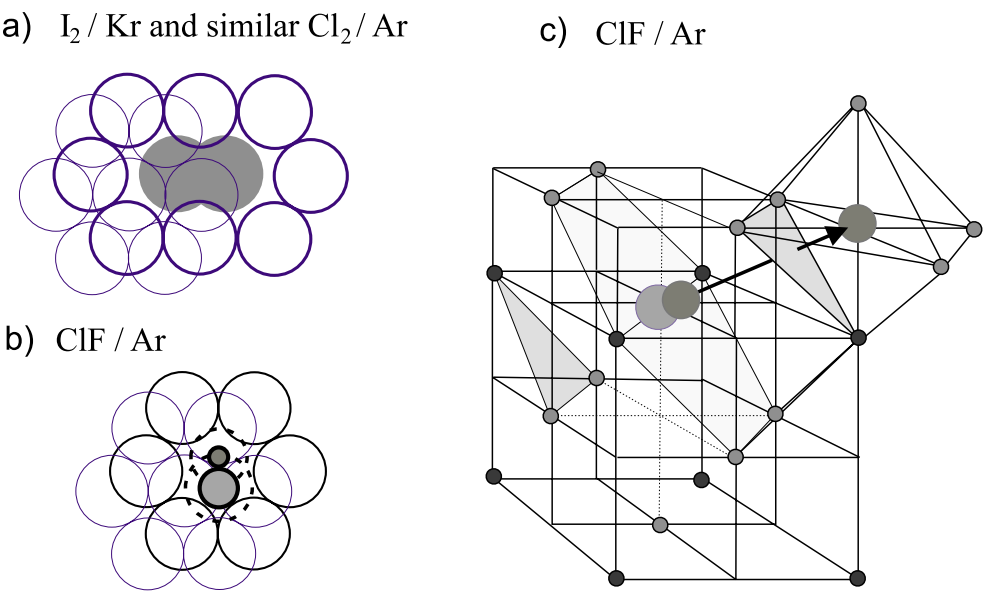

Figure 2.5: a) I_2/Kr matrix. Atoms are indicated with their van-der-Waals radii. I_2 occupies a double substitutional site in the fcc lattice. The situation for Cl_2/Ar is similar. b) ClF is isolated on a substitutional site of the Ar lattice. The van-der-Waals radii of Cl and F are indicated as dashed lines. The shaded cores are the atomic radii. c) ClF in the three dimensional fcc lattice. The F atom is pointing at a triangular window of three Ar atoms. The arrow indicates the direct flight to a nearest interstitial site with octahedral (O_h) symmetry.

the round-trip time is ~ 400 fs (equivalent to 83 cm^{-1}). The anharmonicity of the B state of ClF is $\omega_e x_e = 8.6$ cm^{-1}. A a spectral bandwidth of 300 cm^{-1}, equivalent to a 110 fs excitation pulse, will prepare a wave packet that is dispersed after less than 2 periods ($n = 1.3$).

2.2 Matrix effects and fundamentals

The rare gas matrix – like all solvents – changes the spectroscopy of the isolated molecules in several ways. The electronic polarizability of the medium induces solvational shifts of the electronic states and the nuclear rearrangement of the solvent atoms changes the forces of the solvent cage on the molecule. Within the framework of the DIM and DIIS method (cf. chapter 2.1.3) both effects are treated with good accuracy. This chapter introduces the microscopic physical effects as a basis for the interpretation of the experiments and also for the discussion on the sophisticated simulations using DIM trajectories.

2.2.1 The cage effect and isolation of diatomics in solid rare gases

At low temperatures, rare gases condense into solids, forming an fcc lattice [119]. Molecular and atomic impurities that are co-deposited with the rare gas are usually isolated on single or double substitutional sites of this lattice, depending on their size [6].

When generally speaking, in a condensed phase or in a dense gas, reactant species are in proximity to one another, and are caged in by surrounding molecules, e.g. of the solvent, they may undergo a set of collisions known as encounters; the term ”cage effect”, also known as Franck-Rabinowitch effect, is then applied. In this thesis, the ”cage effect” describes the effect of the rare gas matrix on the dissociation of the isolated diatomics under investigation [36]. The caging is perfect for sterical reasons in the case of I_2 and Cl_2 in solid rare gases, i.e. the dissociation efficiency upon excitation is negligible. On the other hand, small molecules like F_2 and HCl show high probabilities for cage

[6] For certain diatomic impurities an hcp structure is preferred and bigger molecules are isolated in larger vacancies [119].

exit. The light atomic fragments are mobile and may even migrate through the matrix over several nanometers [89, 120]. The onset of thermal mobility of F fragments is 15 K in solid Kr and 25 K in solid Ar [81].

In a potential diagram, the cage effect bends up the potential surfaces when the reactant species approach the cage (cf. Fig. 2.6). A higher potential barrier decreases the cage exit probability, and when the barrier is much[7] higher than the energy of the fragments the cage effect becomes perfect. The origin of the dramatically different cage exit probabilities of I vs. F fragments is pictured in Fig. 2.5. Panels a and b show the individual atoms with their van-der-Waals radii. I_2 in Kr [25] and Cl_2 in Ar [37] occupy double substitutional sites of the fcc-lattice (Fig. 2.5a). Therefore, the fragments undergo head-on collisions with nearest neighbors upon dissociation. Moreover, the I fragments are too big to fit through the spaces between Kr atoms in the lattice. ClF and F_2 in on the other hand, isolate on single substitutional sites. The F fragments point at a triangular window of the fcc-lattice [53] and may exit the cage along the path indicated by the arrow in Fig. 2.5c. It is obvious that the sphere with the van-der-Waals radius of an F atom would not fit through lattice spacing between van–der-Waals Ar spheres that are touching (cf. Tab. 5.3). In reality, the F atoms are able to migrate in solid rare gases, indicating that the picture of F atoms as spheres is too simplified. The open shell fragments have the symmetry of P-orbitals. The electron cloud of the F radicals, which is responsible for the repulsive interaction with the filled electronic shells of the rare gas atoms has less repulsion in the direction of the singly filled P-orbital [68].

Fig. 2.5c displays the situation in three dimensions. ClF is surrounded by its twelve nearest neighbors, and its bond is pointing at the triangular windows (gray shaded areas). The question of whether ClF is fixed in space as indicated in Fig. 2.5c was addressed in a preliminary calculation. ClF is allowed to move, and the first Ar shell is relaxed to find the minimum energy configuration for fixed rotation angle of ClF. The energy is calculated by adding pair-potentials for $Ar - Ar$ [67], $Ar - Cl$ [56], $Ar - F$ [57] and ClF in the ground state [121]. As a result the minimum energy configuration was confirmed to be the one with the Cl and F atoms pointing at opposite triangles of Ar, as indicated in Fig. 2.5c. A barrier of 30 cm^{-1} for adiabatic rotation is obtained, i.e. for rotation of ClF when the Ar atoms have enough time to rearrange to the lowest energy configuration. The full DIM calculation is currently performed in by M. Schröder[8].

2.2.2 Cage exit and isolated F radicals

The dissociation of F_2 and subsequent trapping of F radicals in matrices has been intensively investigated in experiment and theory. A comparison of adiabatic vs. non adiabatic treatment of the P-orbital dynamics in molecular dynamics simulations of F in Kr is discussed in refs. [69,70]. They start from the radiative dissociation of the $Kr_2^+F^-$ exciplex. The fluorescence terminates on a potential surface which provides the Kr atoms with 0.4 eV kinetic energy each and the F fragment with 0.2 eV. After 4 ps the F fragments are stabilized either on an octahedral O_h or a tetrahedral T_d site.

Experiments with dissociation of F_2 in various rare gas matrices were reported [67, 81, 83, 87, 89, 90, 120]. Absorption and emission spectra for F_2/Kr are reproduced and discussed in the respective chapters in Part I of this thesis. Since F_2 is prepared on a single substitutional site, after dissociation the F fragments can occupy - in addition to the O_h or T_d sites - a substitutional site in the lattice. Since Cl mobility is sterically forbidden in matrices, the Cl radical will stay on the original substitutional site after dissociation of ClF. The F atom must accordingly take one of the interstitial sites.

[7] A small tunneling rate may survive, if the barrier is only slightly higher.

[8] Group of Prof. Manz, Theoretische Chemie, Freie Universität Berlin

2.2.3 Electronic polarization

The Onsager model [110, 111, 122] predicts the inductive shift of electronic states as the inductive energy of a molecular dipole $\mu = er$ in a spherical cavity with diameter d in a dielectric with the dielectric constant ε:

$$\Delta E = \frac{1}{4\pi\varepsilon_0}\frac{8(\varepsilon-1)\mu^2}{(2\varepsilon+1)d^3} \tag{2.6}$$

For the valence states μ is approximately constant. The minimum of the potential energy curve, T_e, is a linear function of $(\varepsilon-1)/(2\varepsilon+1)$ [79] and electronic states can be assigned accordingly. The dipole moment μ increases on going from valence to ionic states, and the shift can be quite large for the respective transitions[9]. These shifts due to electronic polarization enter into the discussion in *chapter 5.2* and suggest that the valence states remain unshifted in absorption. The shift in the difference potentials for ClF (*chapter 5.3.1*) is attributed to lowering of the energy of the ionic states.

2.2.4 Nuclear rearrangements

The matrix structurally constrains the molecule, leading to shifts of absorptions and emissions. In a simplified approach, depicted in Fig. 2.6, the potential surfaces can be calculated by adding up pair potentials, e.g. between $Cl-F$, $Cl-Rg$ and $F-Rg$. This is fundamental to understanding the meaning of the effective 1-D potential derived in *chapter 7.1*. The following description exemplifies the "dynamical" potential that results from the additive pair potential approach, used in the molecular dynamics simulations discussed above (chapter 2.1). For the LIF emission a complementary description in a configuration coordinate model is used. Both treatments neglect the electronic effects (i.e. polarization, inductive forces and electronic wave functions) described above.

Model for the dynamic cage

In a system with several coordinates, the one dimensional potential in the coordinate relevant for pump-probe spectra is dynamically changed by the other coordinates. This phenomenon is analyzed in the following. Classical molecular dynamics simulations work with additive pair potentials, i.e. each particle feels the potentials of all other particles. Thus the total potential energy that governs the motion of a diatomic molecule in the matrix is the sum of the molecular potential energy V_{mol} and the energy of the cage potential V_{cage}. The van-der-Waals potential between Rg cage and the molecular fragment X has a shallow minimum and a strong repulsion (Lennard-Jones)[10].

Fig. 2.6 shows the potential energy surfaces of iodine for the three relevant electronic states; the ground state X, the B state, in which the observed dynamics take place, and the E state for the probe transition. They are shown for the gas phase as a thin dash-dotted line. In addition, each state is shown with the potentials imposed by a *static* cage onto the molecular coordinate R. To demonstrate the effect, it suffices to consider an $I-I$ molecule with two Kr atoms in a linear configuration as indicated in Fig. 2.6 (top). The dotted lines, as an example, are calculated as follows. The molecule is in the ground vibrational state of the X state, and the molecular bond is fixed at the corresponding equilibrium position $R_{eq}(X)$. Then the Kr atoms move into the minimum energy configuration, which is given by the van-der-Waals $I-Kr$ distance, i.e. by the shallow minimum of the Lennard-Jones potential. Then the Kr atoms are fixed in this configuration, and the $I-I$ bond is elongated and the total potential energy is calculated as the sum of the $I-I$ and $I-Kr$ potential.

[9] In a second order approximation, the diameter d of the cavity also changes due to rearrangement of the matrix atoms.

[10] This minimum corresponds to what is sometimes called the dispersive forces as opposed to inductive forces, which are induced by a static dipole (e.g. ionic states) on the dielectric. If the weak attraction is neglected, exponential repulsion due to Pauli repulsion of the electronic clouds works fine. These potentials have very short range, rendering a summation over nearest neighbors a good approximation.

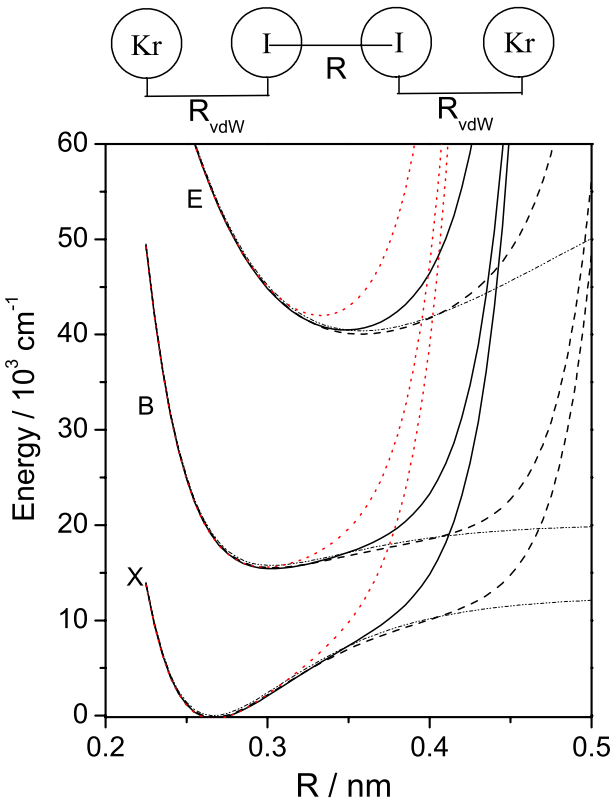

Figure 2.6: a) I_2 molecule with bond distance R and two adjacent Kr atoms at the van-der-Waals distance R_{vdW}. b) Potential energy surface for the ground state X and the excited states B and E. The gas phase I_2 potential is represented by the dash-dotted line. The other curves are additive pair potentials including the two adjacent Kr atoms fixed at the van-der-Waals distance after they have relaxed around the X state equilibrium (dotted), the B state (solid) and the E state (dashed).

The potential bends up at large R, since the I atoms feel the strong repulsion from the fixed Kr. This is a simple account of the cage effect. The solid line is calculated accordingly, now with the Kr atoms fixed in the configuration for the equilibrium position of the B state $R_{eq}(B)$ and the dashed line for the E state configuration. The cage moves outward as the $I-Kr$ repulsion shifts the Kr atoms further away.

As far as molecular dynamics are concerned, the effect of the surrounding matrix can be exemplified in Fig. 2.6 in the following way. Consider the three B state surfaces for the different matrix configurations. In a pump-probe experiment, the pump pulse at $h\nu_{pump}$ prepares the wave packet in the B state in the configuration indicated by the dashed potential for the ground state equilibrium. When the vibrational ($I-I$) wave packet moves outwards to larger R, the matrix cannot stay fixed, but has to respond to the repulsive $I-Kr$ forces. During outward motion, the potential will smoothly change from the dotted to the solid to the dashed shape, and during the inward motion the reverse. Therefore, the effective one dimensional potential, that will be experimentally derived in chapter 7.1.2, looks like an intermediate between the three potentials. Such a potential has up to now not been presented explicitly and instead only potentials for fixed cage geometries are given in the literature, although it would be very helpful for discussions of pump-probe spectra. One way to accomplish this task is proposed in chapter 7.3.1.

It is also instructive to discuss the frequency domain spectroscopy in this picture. If an absorption spectrum is recorded for a molecule in the X state, the Born-Oppenheimer approximation says that the nuclear coordinates will not change in the electronic transition. Therefore, the matrix induces a blue shift in the sense that the minima of the B and E states, $T_e(B)$ and $T_e(E)$, are shifted up due to the repulsion from the Lennard-Jones potential at large R. This effect is clearly visible only for the E state (compare the minima of the dotted and dash-dotted lines). A weak blue shift in absorption with respect to the gas phase is actually seen in the light rare gases, like Ne, where the

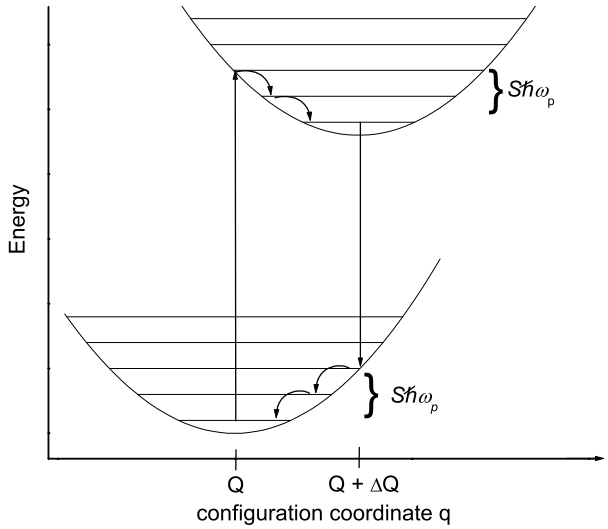

Figure 2.7: Potential energy for two different electronic states in the configuration coordinate model. In the harmonic approximation the potential energy is a parabola with equilibrium position Q for the lower electronic state and $Q + \Delta Q$ for the excited state.

electronic polarization shift to the red is weak [74]. For ionic states the red shift due to polarization overcompensates this weak blue shift.

Note that in the present approximation, all electronic states feel the same $I - Kr$ pair-potential, and for the molecular dynamics calculations, the difference potential ΔV is identical to the gas phase. In different electronic states of a diatomic, the electron clouds have different shapes and this alters the pair interactions to the surrounding atoms. These effects are in part accounted for with the DIM method, but they are small. Comparison of the DIM calculation on I_2/Kr with I_2 gas phase potentials yields variations < 100 cm^{-1} among valence states and < 400 cm^{-1} between ion-pair and valence states.

Electron phonon coupling

The fluorescence from ionic states is the recorded signal in all pump-probe spectra of this thesis. For a proper assignment, their spectroscopy is discussed in *chapter 5.2*. These spectra are usually very broad and red shifted, and the underlying mechanism is discussed in the following. Details are given in refs. [123], [124] and [125].

In the ionic states, the molecular bond is extended compared to the valence states. The strong red shift in emission results from the rearrangement of the rare gas lattice around the larger electronic cloud. To describe the rearrangement of many atoms in a convenient way, a configuration coordinate q is introduced.. It q may be thought of as the size of the cage, for example. In the harmonic approximation, the rare gas matrix forms a parabolic potential (Fig. 2.7) around the molecule in the ground state, $V_g = \frac{1}{2}M\omega_p^2 q^2$, with equally spaced eigenvalues $n\hbar\omega_p$, which are the characteristic phonons of the host lattice (and thus vibrations of the cage). In the excited electronic state of the molecule, e.g. the ionic states, the lattice rearranges around the extended electron cloud. This corresponds to a parabola displaced by ΔQ, i.e. the equilibrium position in the configuration coordinate is larger. In the crudest approximation, the form of the parabola is not changed, implying that the phonon frequency ω_p is kept constant.

In this model the Stokes shift between absorption and emission is $E_s = 2S\hbar\omega_p$ [124, 125]. S is the mean number of phonons emitted during the absorption and the emission [126], and thus a measure of the electron-phonon coupling strength. The creation of phonons is indicated in Fig. 2.7 as the small arrows. S is called the Huang-Rhys phonon coupling constant which is connected to the parabolic potential by the ratio $S\hbar\omega_p = \frac{1}{2}M\omega_p^2\Delta Q^2$. The intensity I of these phonon assisted

transitions is described by a Poisson distribution [127] $I(\hbar\omega_{zp} - n\hbar\omega_{ph}) = e^{-S}S^n/n!$, where $\hbar\omega_{zp}$ is the zero phonon line energy of the electronic transition. This is a consequence of the Franck-Condon overlap of the vibrational wave functions in the two displaced harmonic oscillators [124]. In the strong-coupling limit $(S \gg 1)$, the line shape is Gaussian with the width $H = 2.36\sqrt{S}\hbar\omega_p$. For Cl_2 in Ar it was demonstrated in excitation spectra, that the electron-phonon coupling gradually increases on exciting higher and higher in the part of the anharmonic molecular potential, where the molecular frequency drops below the Debeye frequency of the lattice [128].

2.2.5 Matrix shifts

For different electronic states, molecules and matrices general predictions cannot be made, because the inductive, dispersive and geometrical shifts compete [125, 129, 130]. A collection of shifts for many diatomics in rare gases is given in ref. [74]. The transitions from the ground state to valence states are usually only weakly shifted by 1 to 2 %, since they occur in the Frank-Condon region, where the influence of the matrix is weak. The results on ClF in Ar and Kr presented in *chapter 5.1* lie in the same trend.

For ionic states the strong red shift in absorption is mainly due to the polarization effect, that is described by eq. 2.6. In emission, the rearrangement of the matrix cage yields an additional Stokes shift. Moreover, nonradiative coupling among the ionic states can yield additional red shifts between absorption and emission, when the population relaxes to a lower lying electronic state. Often the coupling is very strong among closely spaced states in the ionic manifold, and the emission usually originates from the lowest state of the ionic manifold.

For completeness: Rydberg states of molecules and atoms are blue shifted in condensed rare gases, since the large Rydberg-electron cloud is repelled by the filled electron shells of the rare gases according to Pauli's exclusion principle. This effect often leads to a deperturbation of the ionic states [131], which in the gas phase strongly couple to the Rydberg states, forming double-well potentials.

2.2.6 Excimers and exciplexes

Excimers are diatomic molecules (dimers) that are bound only in the excited state. Exciplexes are analogous polyatomic molecules (complexes). In the case of rare-gas-halogen molecules, the ground state is only weakly bound (~ 100 cm^{-1} $\sim 1/80$ eV) by van-der-Waals forces, whereas the excited state is ionic and lends its binding energy (several eV) from Coulomb's law. As a typical example consider the potential of KrF is displayed in Fig. 5.5.

These species are largely used in excimer lasers, as they cover a wide range of UV wavelengths and have very large gain [52]. Inversion is easily achieved, since the molecule is not bound in the ground state. Rare gas halides play an important role in the understanding of the chemical bond and are well characterized. Anisotropic potential energy parameters for the diatomics like ArF and $KrCl$ have been derived from molecular beam scattering experiments [56, 57] and ab initio calculations [50, 51]. Triatomic species like Ar_2F and Kr_2F have been calculated ab initio [47–49] and observed in emission in the gas-phase [55] and in rare gas matrices [53, 54] (cf. Fig 4.6).

For pump-probe spectroscopy KrF is an interesting candidate since its absorption is in the near UV. Absorption and excitation spectra of the excimers in Ar and Kr matrices were measured by several groups [82, 88, 132]. The spectra of KrF in Ar agree in all publications and display a well resolved vibrational structure from the levels in the ionic states. The spectra for KrF in Kr are contradictory. While the authors in ref. [132] reported a broad band around 260 nm, a narrow and strong absorption at 275 nm attributed to $Kr_6^+F^-$ dominates the excitation spectrum of ref. [88]. Bressler [82] measured the excitation spectrum and reports both structures, but with a strong yet unexplained dependence on the history of the sample. A series of absorption spectra in *chapter 4.2.4* will clarify the origin of the disagreement and *chapter 4.3.3* offers an explanation.

atom	Cl	F	Ar	Kr	Xe
E^+	12.97	17.42	15.76	14.00	12.13
E^-	3.62	3.40			

Table 2.1: Ionization potentials E^+ and electron affinities E^- of halogens and rare gases

2.2.7 Molecular ion-pair versus excimer states in condensed rare gas

Ionic states involve transferring one electron from one atom to another, and sometimes charge delocalization among several atoms. Let Rg denote rare gas atoms and X and Y halogen atoms. Within this thesis two different ionic species are important. The molecular ion-pair states solvated in rare gas X^+Y^-/Rg or excimers and exciplexes $Y^-Rg_n^+$ with a neutral X nearby. Which of the possible charge distributions is actually taken, depends on the interplay of ionization energy E^+, electron affinity E^- and the polarization energy E_μ of the formed molecular dipole in the dielectric, the energy for charge delocalization E_{del}, as well as the distance-dependent coulomb energy $E_C(R)$ and the "Pauli repulsion" $E_P(R)$ between different atomic orbitals. It is a challenge to accurately model the different species and even more difficult to simulate the dynamics among different species. For some special cases ionic potentials have been calculated in the DIIS formalism [64, 110, 111]. It is considered as an important task for the theoretical collaborations to investigate these states for the F and Cl atoms in rare gases.

Until this is accomplished, the potentials calculated and/or measured in the gas phase have to suffice, and plausibility arguments account for the surrounding matrix and the solvent shift. As an example that will be needed later, consider the formation of Cl^+F^-/Rg vs. $Rg^+F^-\ Cl$. The bond distance of all involved ionic species is approx. 0.25 nm and thus the energy gain in the interplay of E_C and E_P as well as the polarization energy E_μ is approximately equal for both charge distributions. The electron affinity $E^-(F)$ enters equally in both species, and for the moment charge delocalization is ignored. Then the decisive quantity is the ionization potential E^+, which is lower for Cl than for Ar and Kr [11]. In argon the difference in $E^+ = 2.79$ eV (Tab. 2.1). Hence the ionic state Cl^+F^- is observed in argon (*chapter 4.2.1*). Of course, the Ar^+F^- states will be formed, if after dissociation Cl is not near F. The expected formation of Ar^+F^- and Kr^+F^- species in matrices upon F_2 excitation was observed [81, 88]. For Kr and Cl the difference in E^+ is only 1.03 eV. The delocalization of the positive charge among several rare gas atoms cannot be neglected anymore, since the energy is lowered by approx. 1 eV, when $Kr^+F^- \rightarrow Kr_2^+F^-$ [47–49]. The decision whether Cl^+F^-/Kr is stable against formation of $Cl + Kr_2^+F^-$ cannot be made on these grounds (*cf. chapter 5.2.2*).

DIM calculations on these exciplexes [47–49] show that the distance between the Rg atoms in the minimum energy configuration of these exciplexes is much smaller (0.25 nm) than the corresponding $Kr-Kr$ van-der-Waals distances in the matrix. Comparison to the diatomic energies of KrF reveals that the energy of charge delocalization between two Kr atoms is gained only after the bond has shrunk [50, 51]. Therefore, in excitation usually only diatomic exciplexes are important. In emission the $Rg_2^+X^-$ exciplex is observed [81, 88][12].

[11] Only Xe has an even lower ionization energy and therefore the Xe excimers can be used for detection in the OODR experiments [133] (Tab. 2.1). Xe^+Cl^- was also found to exist in matrices [132].

[12] In the ionic states of halogens X^+Y^-, the molecular bond is extended and the rare gas atoms approach the halogen more closely, so that the fluorescence leading to the repulsive halogen-rare gas potential is dramatically red-shifted, as discussed in the preceding chapters. For this reason the states are sometimes assigned as $X^+(Y^-Rg)$ instead of $(X^+Y^-)Rg$ [134]. The ionic species denoted by $(X_2)^-Rg_n^+$ are higher in energy for the relevant molecules in this thesis, since $E^+(Cl) < E^+(Kr)$.

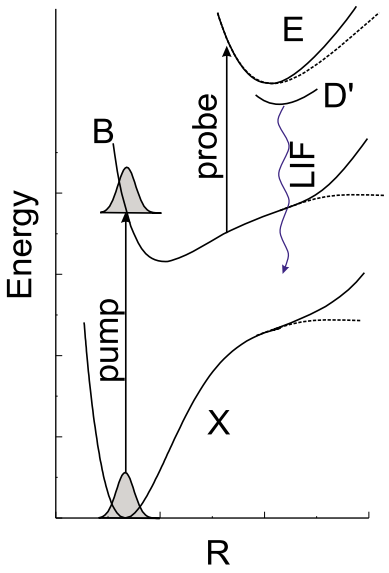

Figure 2.8: Scheme of pump-probe spectroscopy. The dashed lines indicate the gas phase potentials and the solid lines mimic the potentials including the solvent cage effect. The pump pulse prepares a wave packet from a coherent superposition of vibrational levels in the excited electronic state B. The probe pulse promotes the wave packet to the final state E in the ionic manifold, when the packet is in the probe window. After nonradiative relaxation within the ionic manifold, the fluorescence from the D' state is recorded.

2.3 Femtosecond pump-probe spectroscopy

2.3.1 Method

Femtosecond pump-probe spectroscopy is a method to follow ultrafast dynamical processes on the timescale of the pulse duration. The pump pulse starts the dynamics and the probe pulse takes a snapshot of one of the system's properties after a delay time t. The signal can be absorption, or diffraction of the probe photon, or generation of secondaries like fluorescence, photoelectron spectra etc. The signal is recorded as a function of time delay.

In the context of this thesis, femtosecond pump-probe spectroscopy more specifically refers to the process depicted in Fig. 2.8. A fs-pump pulse is absorbed by a molecular system and starts the wave packet dynamics on the excited electronic state, e.g. the B state. The wave packet moves in the potential and when it passes the probe window after the delay time t between pump and probe pulse, it is excited to the E state. The delay time t is varied continuously on the femtosecond timescale. Nonradiative relaxation within the ionic manifold to the D' state results in fluorescence emission (LIF) on the nanosecond timescale[13]. The intensity of the fluorescence as a function of delay time t shows, when the wave packet passes the probe window. In the absence of saturation it is proportional to the intensities of the pump and the probe pulse. The dashed lines in Fig. 2.8 indicate the potentials of the molecules in the gas phase, and the solid curves include the forces from the solvent cage.

The closer analysis of the method needed in the analysis of the spectra requires a more detailed description. The pump pulse creates a wave packet by coherently exciting a superposition of several vibrational states around E_{pump} in an excited electronic state. In the case of a dissociative potential, the continuum of states is coherently excited. The wave packet evolves under the influence of the excited state Hamiltonian. By Ehrenfest's theorems, the expectation values for position and momentum of the wave function satisfy the classical equations of motion (chapter 2.1.5), approximating the motion of a classical particle in a potential, as long as the wave packet is localized. (cf. Fig. 2.9a).

The probe pulse promotes the wave packet to the E state, if the resonance conditions, i.e. energy and momentum conservation, are fulfilled. This is the case when the wave packet is at a probe window position R_{win}, where the difference potential ΔV equals the probe photon energy $h\nu_{probe}$. This condition follows from the Franck-Condon approximation, which is based on a negligible change of the momentum of the wave packet due to the photon [104, 135]. Classical momentum conservation

[13] The fluorescence terminates on several electronic states that are allowed for the dipole transition.

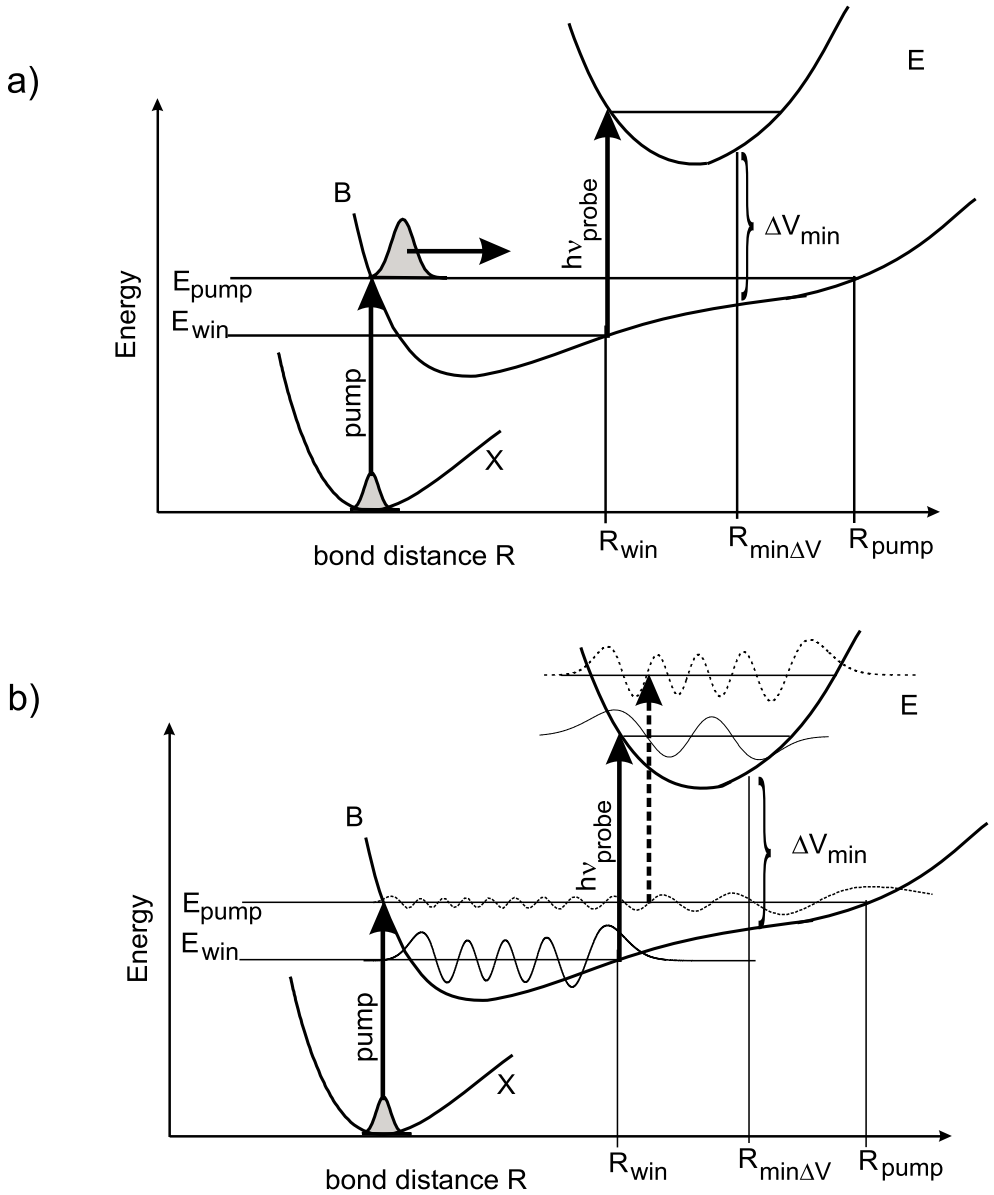

Figure 2.9: Scheme of pump-probe spectroscopy in systems with dissipation. a) The pump pulse prepares a wave packet around E_{pump} in the excited electronic state B. The outer turning point of the wave packet with the initial energy is R_{pump}. The probe pulse promotes the wave packet to the final state E, if the wave packet is at the position of the probe window at R_{win}. The condition for the probe window is that the difference potential $\Delta V = E_E - E_B$ matches the energy of the probe photon $h\nu_{probe}$. The minimum of the difference potential $\Delta V_{\min}$ is located at $R_{\min\,\Delta V}$. The observed pump-probe signal decreases with the velocity, at which the wave packet passes the probe window. At the energy E_{pump} the signal is low. When the wave packet is relaxed to E_{win}, it has zero velocity in the probe window, and the signal is high. b) Same potential diagram including one of the vibrational wave function excited by the pump pulse. It is connected to the vibrational wave function (dashed) in the E state by the probe energy $h\nu_{probe}$ (dashed). The overlap of the wave functions is poor (weak signal). The vibrational wave function at the energy of the probe window E_{win} (solid arrow) has a large overlap to the corresponding wave function in the E state (solid).

requires that the kinetic energy of the wave packet remains unchanged after the electronic transition. The conservation of total energy therefore implies $h\nu_{probe} = \Delta V(R) = V_E(R) - V_B(R)$. A detailed investigation of the classical expression shows that the pump-probe signal is inversely proportional to the velocity[14] v of the wave packet at the probe window R_{win} [45].

The classical argument of momentum conservation is reflected in a quantum description by the overlap integral (Franck-Condon factors) of the nuclear (vibrational) wave functions, corresponding to the vibrational eigenstates that are coherently coupled in the wave packet (cf. Fig. 2.9b). A wave function oscillating quickly with R, corresponds to large kinetic energy (large velocity v) and a slowly varying wave function means small kinetic energy. The overlap of slowly varying wave functions in the initial and final state is large, and the overlap of a fast oscillation with a slowly varying function is close to zero. Two oscillating functions may have appreciable overlap. The overlap of the two wave functions connected with the solid arrow (probe) is large, because the large antinodes overlap and the oscillations do not. This is always the case, if the probe window energy E_{win} is at the energy of the probed level, i.e. the wave packet is probed at the turning point.

In order to deduce information on the dynamics from the pump-probe spectra, the potential, and especially the difference potential ΔV, for the probe transition must be known. As a first approximation, the difference potential is identical to the gas phase in the cases examined here, since the interaction energy of the rare gas atoms with the molecule is similar for all electronic states. This approximation is quite accurate according to the discussion in chapter 2.2.4. In *chapter 7.1* it will be demonstrated, that information from a series of pump-probe spectra can be used to construct a potential energy surface in advance and subsequently extract the dynamics.

2.3.2 The threshold for the probe transition

The probe transition in pump-probe spectroscopy deserves a closer inspection. For a quick discussion consider Fig. 2.9b. It is obvious that no probe absorption will take place if $h\nu_{pump} + h\nu_{probe} < \min E$, i.e. the energy of the vibrational level in the B state prepared by the pump pulse plus the probe energy is smaller than the minimum of the E state. Now let the pump pulse excite vibrational levels around E_{pump} in the B state, above the level needed to reach the region of the lowest probe window at $R_{\min \Delta V}$ (minimum of the difference potential ΔV). Although excited state absorptions with $\min E - E_{pump} < h\nu_{probe} < \min \Delta V$ are energetically allowed, the Franck-Condon overlaps are very small. The high vibrational levels in the B state have fast oscillations with R. The low vibrational levels in E, that could be accessed from the energetics $\min E - E_{pump} < h\nu_{probe}$, vary slowly with R, yielding a poor overlap for all probe energies $h\nu_{probe} < \min \Delta V$ (cf. Fig. 2.9b, dashed wave functions and dashed arrow). This small overlap corresponds to momentum conservation in the wave packet language. The longest probe wavelength that transfers appreciable population to the higher lying E state is given by $h\nu_{\min} = \min \Delta V$. It is determined by the difference potential ΔV and *not* by the difference between the pump energy and the minimum of the final state[15]. This will be used in *chapter 7.1.3* to construct the E state of I_2/Kr.

In order to measure the threshold of the probe transition, i.e. the minimum of ΔV, in the condensed phase, the molecule can be excited with any energy above $E_B(R_{\min \Delta V})$, above the window for the minimum of ΔV. Vibrational relaxation successively populates lower and lower vibrational levels until this level is reached. As long as $h\nu_{probe} < \min \Delta V$, there will be no signal. The resonance is reached for $h\nu_{probe} = \min \Delta V$. This method is applied to obtain the correct vertical shifts of the difference potentials ΔV of ClF and Cl_2 in Ar (*chapter 5.3.1*).

[14] The expression $1/v$ diverges for a wave packet at the turning point and the quantum mechanical expression is needed.

[15] This is the classical result derived above from the Franck-Condon principle. Only a minor correction has to be made to obtain the correct quantum mechanical result, that accounts for the zero-point energy of the zeroeth vibrational level in the E state and the fact that some overlap is already obtained for levels in B that are slightly above $E_{\min \Delta V}$.

2.3.3 Condensed phase pump-probe spectroscopy

In the gas phase, time and frequency domain spectra of a molecule are connected by a Fourier transformation. The information delivered by the two methods is mathematically equivalent. It was exemplified for I_2 that the Fourier transform of a fs-pump-probe spectrum shows the individual vibrational and rotational levels excited by the pump pulse [39]. For a high resolution in the frequency domain, a long pump-probe transient has to be recorded over several 100 ps. In systems with population- and energy-relaxation processes or collision induced decoherence, the oscillations in fs-pump-probe spectra may not live long enough to resolve individual vibrational and rotational levels. This is the case in the system of diatomics in rare gases investigated here. Since the pump pulse excites several vibrational levels, the vibrational frequency measured in a pump-probe spectrum depends on the relative weight with which the individual vibrational levels are probed, i.e. on the probe-wavelength. This effect is experimentally demonstrated very clearly for the first time within this thesis (chapter 7.1.2). It has been noticed previously in classical MD simulations but reported without further discussion [27]. In frequency domain spectra the relaxation processes lead to a broadening of the absorption band, which washes out the relevant structure [29, 62, 100]. This makes fs-pump-probe spectroscopy the method of choice in dissipative systems, since it can beat the timescale of the relevant relaxation processes.

The presence of the solvent or bath changes the pump-probe spectra in several ways. First of all, it induces dissipation and the molecule loses energy (*vibrational energy relaxation, chapter 7.1*). In an anharmonic potential, this changes the vibrational frequency in the course of time (*chapter 7.4.2*). It also changes the envelope of the pump-probe spectrum (*chapter 7.4.1 and 7.4.3*). Often the solvent influences the coupling of electronic states and thus the population relaxation to lower states [42, 43, 66, 115]. The dramatic effect of solvent-induced spin-flip is discussed in *chapter 7.6*. Decoherence, i.e. loss of coherence, is an important issue in the condensed phase. The consequence of decoherence for pump-probe spectra is the loss of modulation depth. Random scattering events of the molecule with the solvent destroy the phase relationship and thus the wave packet. It is important to notice that not only this random dephasing decreases the modulation depth, but also the dispersion of the wave packet due to the anharmonicity of the potential (see above). The decay of this modulation can originate from dispersion (anharmonicity) and decoherence (random collisions) and hence the two processes are often mixed up and called "dephasing" [16]. This situation is complicated by the additional ensemble effect that leads to "inhomogeneous broadening" of the spectral lines and is often also referred to as "dephasing". In principle, the contribution from dispersion can be distinguished from the other processes, because the dispersion on the anharmonic potential can be pre-compensated by chirping the pump pulse, i.e. by negative optical dispersion introduced in the pump-pulse. A short discussion on coherence vs. dephasing in the measured spectra can be found in *chapter 7.9*.

It should be mentioned that LIF detection in pump-probe spectroscopy has the advantage in condensed phases that this method probes the population of the excited state in the coordinate of the probe transition. The observed fluorescence signal is proportional to the population in the final state after both pulses, and measures the diagonal elements of the density matrix in the excited state. The method of coherent anti-Stokes Raman scattering (CARS), for example, measures coherences, i.e. off-diagonal elements. Moreover, CARS requires an electronic coherence, which decays rapidly in condensed phases (~ 100 fs) and damps out the oscillations [58, 62, 136]. The LIF technique allows the observation of oscillations due to vibrational coherence, even if electronic dephasing is very fast.

[16] It is unfortunate that in the most widely used theoretical framework, especially for MD in the liquid phase, all quantities are expressed as correlation functions, which do not distinguish decoherence and dispersion. For the calculation of the pump-probe spectrum, this correlation function is the overlap of the ground state Gaussian with the excited state wave packet.

2.3.4 Selection rules

In light diatomic molecules like ClF the angular-momenta are coupled according to Hund's case a, and the following selection rules hold [137]: $\Delta S = 0$, $\Delta\Sigma = 0$, $\Delta\Lambda = 0, \pm 1$ and from $\Sigma + \Lambda = \Omega$ it follows that $\Delta\Lambda = \Delta\Omega$. Therefore a transition ${}^1\Sigma_0 \rightarrow^1 \Pi_1$ is allowed, whereas ${}^3\Pi_0 \rightarrow^3 \Pi_1$ is forbidden. Optical transitions between singlet and triplet states are spin-forbidden (spin selection rule: $\Delta S = 0$), transitions with $\Delta\Omega = \pm 2$ are dipole-forbidden and originate from the quadrupole-interaction with the light field. The transition $X({}^1\Sigma_0) \rightarrow B({}^3\Pi_0)$ is spin-forbidden $(\Delta S = 1)$,but the selection rule is weakened by the spin-orbit interaction[17]. In the heavy I_2 molecule the angular momenta are coupled according to Hund's case c, and only the selection rule $\Delta\Omega = 0, \pm 1$ remains [137].

The selection rules are reflected in the transition moments that have been calculated by A.B. Alekseyev (cf. Fig 5.6) and in part published in ref. [121]. They will be used in *chapter 5.3.1*. Transitions between valence and ion-pair states are governed by the propensity rule $\Delta\Omega = 0$, since they involve transferring an electron from one atom to another. To accomplish this, an electric field in the direction of the electron transfer is needed. In a diatomic the transition is parallel to the molecular axis, i.e. $\Delta\Omega = 0$. The electronic states in Fig. 2.11 and 4.1 have been labeled according to their quantum number Ω for that reason. This propensity rule is valid also for I_2.

The following considerations on polarization are important for the polarization selective pump-probe spectroscopy discussed in *chapter 7.5*. In analogy to the Zeemann effect in atoms, where m_j is the projection of the angular momentum j on the axis of symmetry dictated by the magnetic field, Ω is the projection of the electronic molecular angular momentum J on the internuclear axis. For observation transverse to the symmetry axis, $\Delta m_j = 0$ and $\Delta\Omega = 0$ correspond to polarization parallel to this axis and $\Delta m_j = \pm 1$ and $\Delta\Omega = \pm 1$ to perpendicular polarization. For longitudinal observation, only $\Delta m_j = \pm 1$ and $\Delta\Omega = \pm 1$ exist, since the polarization is perpendicular to the symmetry axis [138]. The difference for the molecule from the Zeemann analogy is that, for the Stark effect induced by the internuclear electric field, the emitted light is not circularly polarized, since the effect of the electric field is the same for electrons with $m_j = \pm 1$ [139]. The interplay of polarization and selection rules gives rise to the method of photoselection [140]. Electronic excitation with polarized light prepares a distribution of excited-state molecules aligned with the light polarization $(\Delta\Omega = 0)$ or perpendicular to it $(\Delta\Omega = \pm 1)$ (cf. chapter 2.3.5)

2.3.5 Polarization dependent pump-probe spectra

This chapter provides the intensity ratios for the LIF expected in polarization sensitive pump-probe spectra that were taken for the analysis of angular reorientation in *chapter 7.5*. Electronic transitions in molecules have a transition dipole moment with magnitude and direction. The transition dipole matrix element $| < \Phi_i | \overrightarrow{E} \cdot \overrightarrow{\mu} | \Phi_f > |^2$, which determines the intensity of absorbed or emitted light, is proportional to the square of the scalar product $\overrightarrow{E} \cdot \overrightarrow{\mu}$, where $\overrightarrow{\mu}$ is the transition dipole and $\overrightarrow{E}$ is the electric field. If a sample of randomly oriented molecules is excited with linearly polarized light, an ensemble of molecules is selected that have the transition dipole aligned with the polarization (photoselection [138, 140]). The analytic form of the dipole distribution is $\cos^2\theta$ (Fig. 2.10b), where θ is the angle between the electric field $\overrightarrow{E}$ and the transition dipole $\overrightarrow{\mu}$ [138].

If the transition dipole moment in a diatomic molecule is directed along the internuclear axis, the transition is called parallel $(\Delta\Omega = 0)$, otherwise perpendicular $(\Delta\Omega = \pm 1)$ (cf. chapter 2.3.4). A parallel transition yields an ensemble of molecules with an alignment of the axes that is identical to the distribution of dipoles (Fig. 2.10b). A perpendicular transition selects an ensemble of molecules

[17] Since $\Delta\Lambda = 1$ it follows from $\Delta\Omega = 0, \pm 1$ that the transition is to the $\Omega = 0 + \Delta\Lambda \pm \Delta\Sigma = 0$ state (unlike $X\,{}^1\Sigma_0 \rightarrow^1 \Pi_1$).

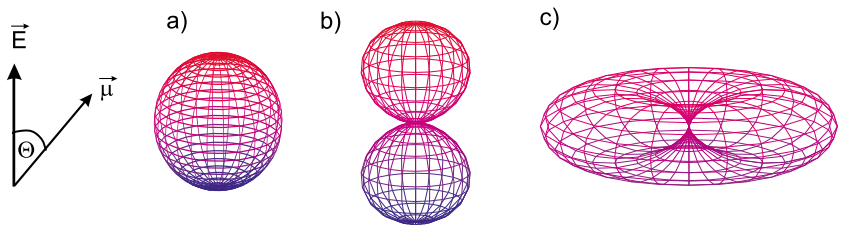

Figure 2.10: Distributions of the molecular ensemble, a) sphere for a randomly distributed ensemble, b) ensemble selected with polarized light in a parallel ($\Delta\Omega = 0$) transition, c) ensemble selected with polarized light in a perpendicular ($\Delta\Omega = \pm 1$) transition.

with the axis perpendicular to the $\cos^2\theta$ distribution, i.e. a toroidal ensemble of molecules, $\sin^2\theta$ (Fig. 2.10c).

If the molecules do not rotate or librate, they will fluoresce with a well defined polarization, i.e. they emit a photon with polarization along the transition dipole for emission[18]. This is used in fluorescence depolarization spectroscopy to determine the angular motion of molecules on the timescale of the fluorescence lifetime by recording the fluorescence anisotropy as a function of time.

This thesis deals with the polarization dependence[19] of the photons absorbed and emitted in forward direction. The photoselected anisotropy is detected with a polarization analyzer or, equivalently, by another interaction with a polarized photon[20]. For general theory on polarization dependent spectroscopy the reader is referred to ref. [141].

For convenience, Tab. 2.3.5 collects the possibilities for two or three interactions of a molecular ensemble with a light field that are relevant to the pump-probe experiments presented in this thesis. The transition dipole moment $\overrightarrow{\mu}$ of the pump transition can be parallel (Fig. 2.10b, $\cos^2\Theta$) or perpendicular (Fig. 2.10c, $\sin^2\Theta$) to the molecular axis. This is indicated by the lobe "8" and the torus "◎" in the first column of Tab. 2.3.5. The probe transition and the fluorescence are parallel transitions ($\Delta\Omega = 0$) in all cases examined here, since they have charge transfer character (cf. chapter 2.3.4). The polarization of the probe pulse is fixed ($\|$, column three), e.g. parallel to the optical table. The pump pulse has perpendicular ($\perp$) or parallel ($\|$) polarization with respect to the probe pulse, or the distribution is randomized (o). Column four specifies whether no polarization analyzer is used ("O") or whether it is perpendicular $\perp$ or parallel $\|$ to both pulses.

A quick graphical explanation for the expected intensity ratios that are collected in the last column can be given as follows. Since all photons propagate in the forward direction, each interaction of the transition dipole with a light field (emission or absorption) mathematically corresponds to calculating the overlap of the three distributions in Fig. 2.10, when their volumes are normalized to 1. The distribution b) has to be rotated by 90° when calculating the overlap for perpendicular $\perp$ photoselection or LIF analyzer. Alternatively the values can be looked up in ref. [141].

Experiments are often carried out in the magic angle configuration, with the two relevant polarizations at an angle of 54°. At this angle the signal is independent of the orientation of transition dipoles [142].

[18] In the diatomic molecules examined here, the transition dipole in emission has the same direction as in absorption.

[19] Dipole radiation is anisotropic both with respect to the direction of the emitted or absorbed photon and to their polarization. A dipole emits and absorbs radiation with a toroidal intensity distribution for the direction of the emitted light as shown in Fig. 2.10c (theory of Hertz oscillator), and the polarization has a $\cos^2\Theta$ distribution (Fig. 2.10b). Thus, the anisotropy after polarized excitation can be simply recorded by comparing the emission in forward direction with the one in the direction of the exciting polarization.

[20] A polarization analyser selects the emitted photons with the right polarization in emission and an incoming photon is polarized before the interaction.

transition dipole for pump	photo-selection	probe transition	LIF analyzer	intensity
parallel 8	$\parallel$	$\parallel$	O	$I_{\parallel} = 3/5 = 0.6$
parallel 8	$\perp$	$\parallel$	O	$I_{\perp} = 1/5 = 0.2$
parallel 8	o	$\parallel$	O	$I_d = 1/3 \approx 0.33$
parallel 8	$\parallel$	$\parallel$	$\parallel$	$I_{LIF\parallel} = 5/35$
parallel 8	$\parallel$	$\parallel$	$\perp$	$I_{LIF\perp} = 1/35$
perpendicular $\circledcirc$	$\parallel$	$\parallel$	O	$1/5 = 0.2$
perpendicular $\circledcirc$	$\perp$	$\parallel$	O	$2/5 = 0.4$

Table 2.2: Intensity ratios observed for spectroscopy with polarized light. Pump and probe pulse are collinear and the fluorescence is observed in the forward direction. The first column denotes whether the electronic transition is parallel 8 ($\Delta\Omega = 0$) or perpendicular $\circledcirc$ ($\Delta\Omega = 1$). The second column specifies the photoselection of the originally isotropic ensemble by the pump pulse, with polarization parallel $\parallel$ or perpendicular $\perp$ to the probe polarization, which is kept fixed (third column). o indicates an isotropic (depolarized) ensemble. The fourth column specifies the polarization of the fluorescence detection with respect to the probe. O indicates no polarization analyzer. The abbrevations $I_{\parallel}$, $I_{\perp}$, I_d, $I_{LIF\parallel}$ and $I_{LIF\perp}$ together with the respective intensity ratios are given in the last column.

2.3.6 I_2 in Kr as the model system to advance fs-pump-probe spectroscopy in the condensed phase

One part of this thesis is dedicated to pump-probe spectroscopy on I_2 in Kr matrices. This system is particularly well studied and characterized. Its heavy mass makes I_2 a convenient molecule for fs-pump-probe studies. The focus of the part of the thesis concerning I_2 is to test the power of the ultrafast spectroscopic tool and to learn how detailed information on molecular dynamics can be extracted from the spectra without the help of simulations. This chapter gives a concise introduction to the relevant previous work on I_2.

A series of pioneering publications by the Zewail group [42–44] investigated the influence of rare gas environments on the free molecule, in clusters and in the gas phase for increasing rare gas pressures up to liquid phase densities. The observed number of oscillations decreases with increasing rare gas density and this was in part attributed to a rapid loss of B state population due to predissociation, i.e. nonadiabatic transitions to a dissociative state. Surprisingly strongly modulated wave packet oscillations extending up to several ps with up to 20 periods were observed in the ordered crystalline phase of Ar, Kr and Xe matrices in the Apkarian group. A wealth of information on energy relaxation and predissociation dynamics induced by the cage was derived from the experimental data in combination with classical trajectory calculations [21, 23, 25–29, 45, 58, 62]. Semiclassical calculations on DIM surfaces [63–65] corroborate essential features. Focusing of wave packets in the B state of I_2 in Kr after several ps was achieved by linearly chirped pump pulses [31, 32].

Absorption and emission spectra of I_2/Kr are well known. In this thesis the B state is excited in the Franck-Condon region from 570 to 480 nm, the $B \rightarrow E$ transition is used as the probe and the $D' \rightarrow A'$ transition at 420 nm is monitored together with $\beta \rightarrow A$ for the pump-probe spectra [80, 115]. The B state in matrices shows a peculiarity. While the vibrational dynamics in pump-probe spectra are well resolved it is not possible to derive the essential spectroscopic constants like T_e, ω_e and $\omega_e x_e$ from absorption spectra because only a structureless Franck-Condon envelope is observed. This is explained by long lasting $I-I$ correlation functions and quickly damped I_2-matrix and matrix-matrix correlation functions [62].

This situation provides a challenge and a test bed to derive the spectroscopic properties from fs-pump-probe spectra. While for free molecules it was especially demonstrated in the I_2 case [39] that

the Fourier transformation of fs and ps data is equivalent to analyzing rotationally resolved vibrational progressions [143], this method requires modifications for the strong interactions in condensed phases which in many cases lead to fast vibrational relaxation. A wave packet started at high vibrational levels falls down within a few oscillations in the potential well, thus passing quickly through regions of rather different frequencies, prohibiting a standard Fourier transformation.

For this case it was shown [32, 144] that by following the decrease in duration of the vibrational periods along the time course of a pump probe spectrum and by systematically varying the pump photon energy, i.e. the starting point in the potential well, it is possible to derive both the spectroscopic constants and the vibrational relaxation rates.

This thesis works out the concept in more detail, and shows especially that accurate spectroscopic constants also require a systematic variation of the probe photon energy (*chapter 7.2*). The determination of vibrational relaxation rates relies on the anharmonicity, which becomes small near the bottom of a bound potential energy surface. The periods have to be measured more and more accurately with decreasing anharmonicity and energy relaxation rate. An improved B state potential energy surface up to the dissociation limit is derived that includes the dynamics of the solvent cage. This potential is an effective 1-D-potential that should be observed in DIM-trajectory calculations, if the energy is averaged over all trajectories, as detailed in *chapter 7.3.1*. Shifting the spatial position of the probe window near the dissociation limit directly yields snapshots of an experimental $R(t)$ trajectory at large elongation R of the $I-I$ bond. The trajectories and the derived kinetic energies display the details of the caging of the I atoms by the matrix atoms.

2.4 The molecule chlorine monofluoride (ClF)

The spectroscopy of F_2 in rare gases shows that electronic transitions in this system lie unfavorably far[21] in the UV, rendering femtosecond pump-probe experiments difficult. The ClF molecule possesses the interesting F fragment which is mobile in matrices, but has advantageous spectroscopic properties as will be shown in this thesis.

2.4.1 Chemical and physical properties

The ClF molecule is the lightest interhalogen, with atomic masses $m(Cl) = 35$ amu and $m(F) = 19$ amu. The colorless gas is used in chemical industry as a strong fluorinating agent and is sold commercially in large quantities but also in $1\ l$ bottles with a purity of 99%[22]. The melting point of ClF is $T = 117.55$ K and the boiling point is $T = 173.15$ K. In contact with water it decomposes to hydrofluoric and hydrochloric acid (HF and HCl). ClF is formed at $250°C$ in the presence of copper as a catalyst by the reaction sequence $Cl_2 + 3F_2 \rightarrow 2ClF_3$ followed by $ClF_3 + Cl_2 \rightarrow 3ClF$ [91]. The molecule is stable at room temperature against decay into $Cl_2 + F_2$ and a slight excess of Cl_2 prevents the disproportionation $3ClF \rightarrow Cl_2 + ClF_3$. Therefore, most of the 1% impurity in the gas used is Cl_2.

2.4.2 Spectroscopy and potential

Despite the stability and commercial availability only little spectroscopic information on gas phase ClF was available before V. A. Alekseev *et al.* investigated this molecule using optical-optical double resonance (OODR) spectroscopy [133, 145–148]. Merging their experimental work with the recent configuration interaction (CI) calculations by A. B. Alekseyev *et al.* [121] has resulted in very accurate potential surfaces for gas-phase ClF (see Fig. 2.11).

[21] Especially the probe to the ionic states would be 4.45 eV further to the UV, due to the higher ionization potential of F compared to Cl (cf. Tab. 2.1).

[22] Sold by ABCR GmbH & Co KG, Hansastr. 29c, 76189 Karlsruhe, Germany.

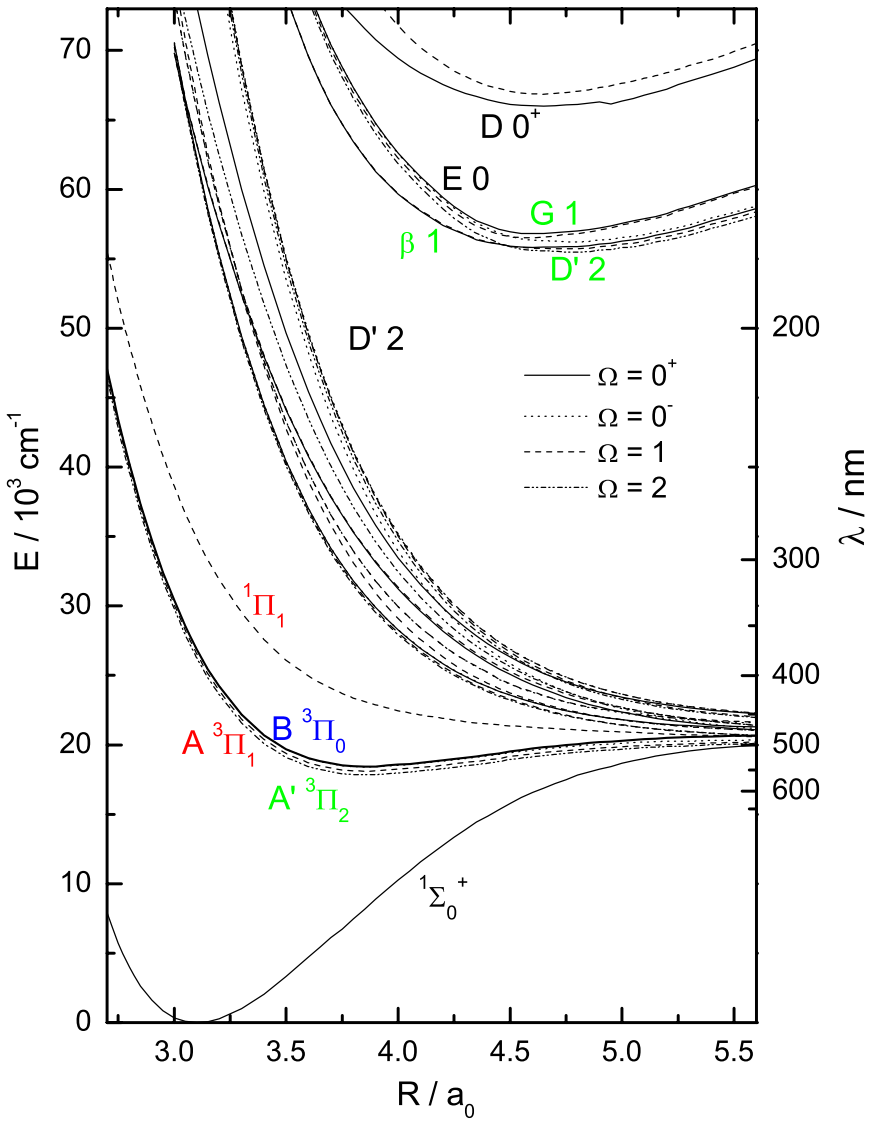

Figure 2.11: Potential of ClF from ref. [121]. The line structure represents the quantum number $\Omega = 0^+$ (solid), $\Omega = 0^-$ (dotted), $\Omega = 1$ dashed and $\Omega = 2$ (dash-dot).

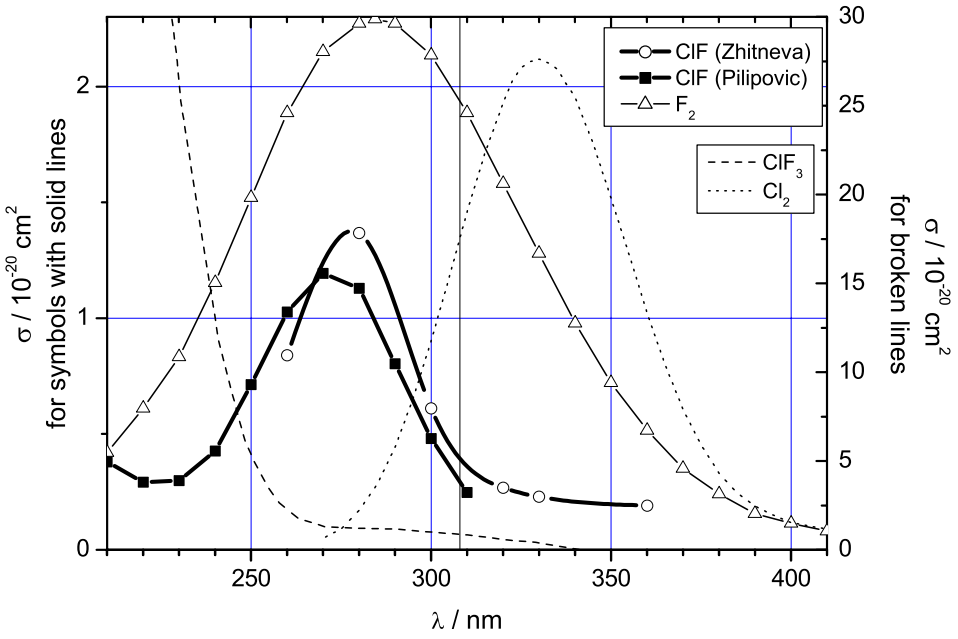

Figure 2.12: Absorptions of ClF, Cl_2, F_2 and ClF_3. The scale on the left hand side is for solid lines with symbols, ClF (open circles after Zhitneva [150]), ClF (solid sqares after Pilipovich [149]) and F_2 (open triangles [151,152]). The scale on the right hand side is for the stronger absorbing molecules Cl_2 (dotted [153]) and ClF_3 (dashed [154]).

Electronic absorption spectra in the dissociation continuum of ClF are given in ref. [149, 150] for the range from 190 to 360 nm and reproduced in Fig. 2.12. The maximum of the absorption is around 270 to 280 nm with a weak cross section of $\sigma = 1.36 \times 10^{-20}$ cm^{-2} (ref. [150], open circles) or $\sigma = 1.21 \times 10^{-20}$ cm^{-2} (ref. [149], solid squares).

In a third paper [155] the absorption band at 270 nm is shifted to 250 nm and stronger by a factor of 8, probably due to a Xe impurity. A comparison to a calculated absorption spectrum gives confidence in the above mentioned spectra (cf. Fig. 5.2). The separation from impurities Cl_2, F_2 and ClF_3 is difficult according to Fig. 2.12. Despite the weak absorption in the bound state $B(^3\Pi_0)$, a laser excitation spectrum has been reported by I. S. McDermid [156] and references for the pioneering work on the ClF molecule are given therein. The spectroscopic data for the ground state obtained by various methods are collected in Ref. [157] and reproduced in Tab. 5.1. The relative absorption cross sections ($\sigma \sim \mu^2$) for the B and $^1\Pi$ state can be estimated from the transition moments μ that were kindly provided by A.B. Alekseyev [158]. The ratio of the respective maxima yields $\sigma(X \rightarrow {}^1\Pi_1)/\sigma(X \rightarrow B(^3\Pi_0) = 50$ (cf. discussion in chapter 5.1.2).

The value for the fundamental frequency $\nu_{0\rightarrow 1}$ of the ground state is taken from IR absorption data [159] that have been reinvestigated by J. A. Coxon [160]. The ground state vibrational progression characterized by the frequency ω_e and anharmonicity $\omega_e x_e$ are derived from electronic absorption and emission data of the $X \leftrightarrow B$ transition [157].

Several articles concerning IR and Raman spectra of ClF in condensed media have been published. The first [161] was on ClF in solid Ar and N_2. L. Andrews reported more details on infrared spectra of ClF in rare gas matrices at a dilution of 1:50 [162]. In addition to the slightly shifted ground state vibrational frequencies of 770.2 cm^{-1} and 762.7 cm^{-1} for the two isotopes (in Ar) additional

peaks were observed and attributed to dimers and higher clusters. The frequency of a matrix-isolated ClF-monomer is shifted to the red by approximately 3 cm^{-1} in Ar and 10 cm^{-1} in Kr as compared to the gas phase values [157]. Similar red shifts have been reported for ClF in liquid Ar (5 cm^{-1}), O_2(6 cm^{-1}) and N_2 (8 cm^{-1}) [163].

Spectroscopy on the ionic states is performed by the OODR technique [133, 145–148] and the emission $D' \rightarrow A'$ has been used to construct a laser at $\lambda = 284.4$ nm [164–166]. Absorption spectra for the lowest Rydberg states [167] of ClF (140 - 129 nm) can be compared to calculations [168].

Several publications report very precise experimental [169, 170] and theoretical [109] studies of the ground state of the triatomic van-der-Waals complex $ArClF$, showing deviations of the potential from simply adding pair-potentials, and reveal three-body effects. The effects are quite small but may play a role in the initial alignment of the ClF molecule in the Ar matrix (see end of chapter 2.2.1).

2.4.3 Photochemistry of ClF

Few experiments on the photochemistry of ClF in the gas phase have been reported. Photodissociation of ClF_3 yields F and Cl atoms [171] and the photolytic reaction $3ClF \rightarrow Cl_2 + ClF_3$ was investigated by Zhitneva [150]. Two-photon laser assisted reactions with Xe produce the excimers $XeCl$ and XeF [155, 172] and these species are used in the OODR experiments to detect the formation of the ion-pair states of ClF [133, 145–148].

Two reviews on photochemistry in matrices deal especially with the reactions of F fragments in Ar and Kr [36, 86]. In an early matrix study the $F - Cl - F$ radical was investigated in solid nitrogen, since it is interesting for chemical structure considerations of a 21 electron system [173–175]. Complexes and photoreactions of ClF with metal atoms [176], with hydrogen [177] and with oxygen were studied by IR spectroscopy and UV absorption [178].

2.4.4 Stable triatomic rare gas halides in the ground state

Some rare gas halide trimers of the form RgX_2 form stable molecules. XeF_2 is a white powder at room temperature. KrF_2 is calculated [179] to be stable by 0.39 eV and the experimental value is 1.01 eV [92–94]. It has been observed in matrices by IR and Raman spectroscopy as well as the molecule $ClXeF$ [95]. The same experiments that tried to prepare $ClKrF$ did not have a positive result, although the species is predicted to be stable [97]. The linear molecule Kr_2F was observed by ESR spectroscopy [180]. These molecules may be important in future experiments, when the fs-control of photochemical reactions is pursued further.

2.4.5 Electronic states of interhalogens: ClF

Halogen and interhalogen molecules exhibit a simple electronic structure. The constituent atoms have a single p-hole in the outer shell, giving rise to states which are equivalent to those from only one outer shell electron. The orbital diagram for ClF is shown in Fig. 2.13. The F atom has higher electron affinity and thus the binding molecular orbitals σ and π have higher probability near the F atom, whereas the antibinding orbitals are closer to Cl. [181]. In the correlation diagram the interhalogens are close to the separated atom model [137, 139].

The electronic *states* of a molecule, e.g. Σ, Π, Δ, result from occupying the molecular orbitals with electrons. The ground state $X(^1\Sigma_0)$ of ClF is a singlet state, because all spins are paired up when the five p electrons of F and Cl occupy the lowest possible molecular orbitals as shown in Fig. 2.13. The symmetry Σ comes from the unoccupied σ^* orbital. The lowest valence states are $1^3\Pi$ and $1^1\Pi$. They originate from an excitation $\pi^* \rightarrow \sigma^*$, thus the total orbital angular momentum of

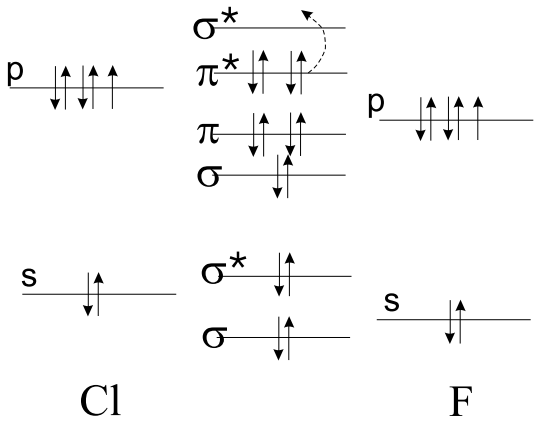

Figure 2.13: Orbital diagram of ClF. The atomic s and p orbitals of Cl and F are occupied with seven electrons each. In the ground state all molecular orbitals, except the antibinding σ^* are occupied with a pair of electrons. The excitation of one electron from π^* to σ^*, indicated by the dashed arrow, gives rise to the lowest lying excited states.

the unoccupied orbitals is $\Lambda = 1 + 0$. The two spins can be either parallel or antiparallel (triplet or singlet)[23].

The following paragraphs summarize and extend the discussion of the orbital character of the different states from the recent publication on CI calculations on ClF by A. B. Alekseyev *et al.* [121]. Potential curves are given for all 23 valence states and 9 ion-pair states. In the Franck Condon region, the most stable electronic configuration is the $\sigma^2\pi^4\pi^{*4}$ closed-shell species, which produces the strongly bound $X(^1\Sigma_0)$ ground state. The σ orbital has binding character, while its counterpart, the lowest-lying unoccupied σ^* orbital, is antibinding . In the Franck Condon region, the π and π^* orbitals are also binding and antibinding , respectively, though much more weakly so in comparison with the σ and σ^* MOs. They become nearly lone-pair $p_{x,y}$ orbitals localized on the F and Cl atoms at intermediate distances larger than 4.0 a_o. The ground state dissociation energy can be estimated from the calculated energy value at a large ClF separation, $r = 20.0\ a_0$, which gives $D_e = 20878$ cm$^{-1} = 2.589$ eV. The upper limit derived in experimental studies from the predissociation of the B state [156, 182] caused by the interaction with a repulsive 0^+ state is $D_0 < 21126 \pm 6$ cm^{-1}.

All other eleven valence states result from the π^*, π or $\sigma \rightarrow \sigma^*$ excitations relative to the $\sigma^2\pi^4\pi^{*4}$ ground state configuration. The lowest two ClF excited states are $1^3\Pi$ and $1^1\Pi$ ($\sigma^2\pi^4\pi^{*3}\sigma^*$ in the Franck-Condon region), which correspond to the $\pi^* \rightarrow \sigma^*$ transition with the lowest excitation energy (Fig. 2.13). The $1^3\Pi$ multiplet is the only ClF excited state which is bound, by approximately 2700 cm^{-1} without spin-orbit coupling, and is characterized by a much larger equilibrium distance, 3.9 a_o vs. 3.07 a_o for $X(^1\Sigma_0)$. It is worth noting that at a bond length of 3.9 a_o the π and π^* MOs are almost completely localized on the F and Cl atoms, respectively, and thus have nonbinding character. This means that the $1^3\Pi$ state arises from excitation out of the nonbinding π^* to the antibinding σ^* orbital, which explains its much smaller binding energy relative to the ground state. The $\sigma^2\pi^4\pi^{*3}\sigma^*$ configuration dominates the 1 $^3\Pi$ state up to its equilibrium distance, where contributions from the $\sigma^2\pi^3\pi^{*4}\sigma^*$ ~18.0% and $\sigma^1\pi^4\pi^{*3}\sigma^{*2}$ ~28% configurations also become important, with their influence quickly increasing at longer distances. The same type of behavior is also characteristic for the $1^1\Pi$ state, for which the exchange of leading configurations happens at slightly shorter distances. This state has a flat potential curve, with a very shallow minimum of approximately 100 cm^{-1} depth at 6.5 a_o.

When the molecular bond is broken in these lowest electronically excited states, the atomic fragments dissociate into ^2P states. Since the F has higher electronegativity the σ^* hole stays with the F, as this corresponds to lower energy than the π^* hole, which stays at the Cl. Geometrically, the singly occupied atomic P orbitals are oriented as shown in Fig. 2.14. At large internuclear distances

[23]The 1 before $^1\Pi$ is the principal quantum number and counts the number of nodal planes in the wave function. 1 corresponds to one nodal plane at infinity (ref. [137] p. 326).

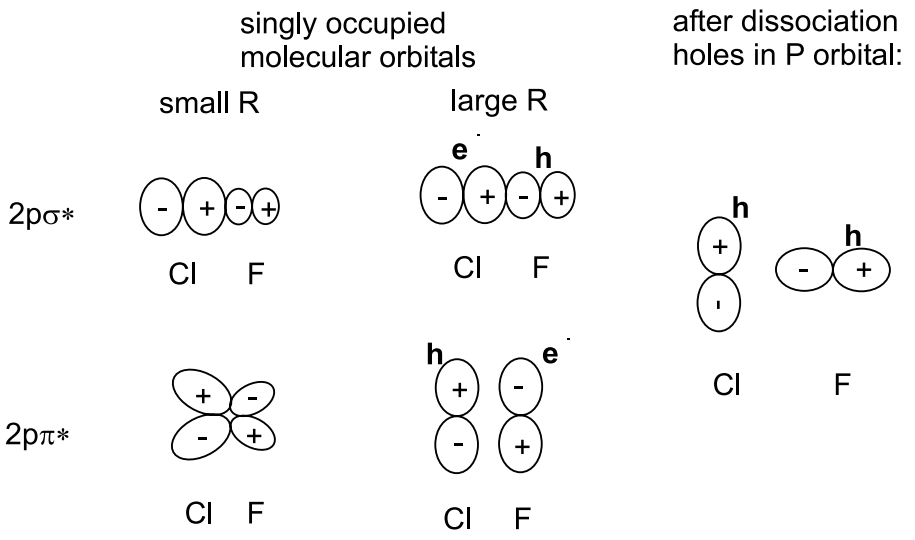

Figure 2.14: Molecular orbitals for dissociation in the first excited state manifold of ClF. The two antibinding singly occupied molecular orbitals of ClF tranform to atomic orbitals localized on Cl and F. The $p\pi^*$ orbital is a lone pair already for $R > 3.9\ a_0$. Since F has higher electronegativity, the hole (h) in the highest molecular orbital σ^* stays with F during dissociation. The singly occupied P-orbital on the F atom is accordingly oriented parallel to the direction of motion. The Cl is left with the hole in an orbital perpendicular to this direction.

$R > 3.9$ a$_0$, the molecular π orbitals already resemble lone-pair $p_{x,y}$ orbitals. The singly occupied P orbital of the F atom ($2p\sigma^*$) points in the direction of the dissociative motion, whereas the Cl orbital is perpendicular to it ($2p\pi^*$). After dissociation, the Cl and F radical are left with seven electrons in the outer shell, each. The singly occupied P orbitals on Cl and F, i.e. the ones which are left with a hole, are oriented perpendicular and parallel to their direction of motion, respectively. This will influence the encounters with the solvent atoms, and the picture helps to visualize the processes in the scattering and spin-flip dynamics in *chapters 7.5.3* and *7.6*.

There is a large gap in the ClF electronic spectrum, up to an excitation energy of approximately 55 800 cm^{-1}, at which the first two of the ion-pair states, $3\,^3\Pi(\sigma^2\pi^4\pi^{*3}\sigma^*)$ and $2\,^3\Sigma^-$ ($\sigma^2\pi^4\pi^{*2}\sigma^{*2}$), appear. They converge to $Cl^+(^1P) + F^-(^1S)$ of the separated atoms. Both of them are strongly bound, mainly due to the $Cl^+ - F^-$ electrostatic interaction, which explains their long equilibrium distances with respect to the ClF ground state. The transitions to these states are used to monitor the recombination dynamics of ClF/Ar, and the shifted difference potentials to the valence states are given in *chapter 5.3.1*. The highest-lying states considered in ref. [121] are the singlet ion-pair states $^1\Sigma^+$, $^1\Pi$ and $^1\Delta$, all converging to the $Cl^+(^1D) + F^-(^1S)$ dissociation limit. They have very similar potential curves with approximately 10000 cm^{-1} higher excitation energies and will not be excited in this thesis, however, will be important to study $^1\Pi$ state dynamics more closely, which lead to rapid spin-flip (*chapter 7.6*).